Cell Reports
Medicine

Article

Histone methyl-transferase G9a inhibition boosts the efficacy of immune checkpoint inhibitors in experimental hepatocellular carcinoma

Graphical abstract

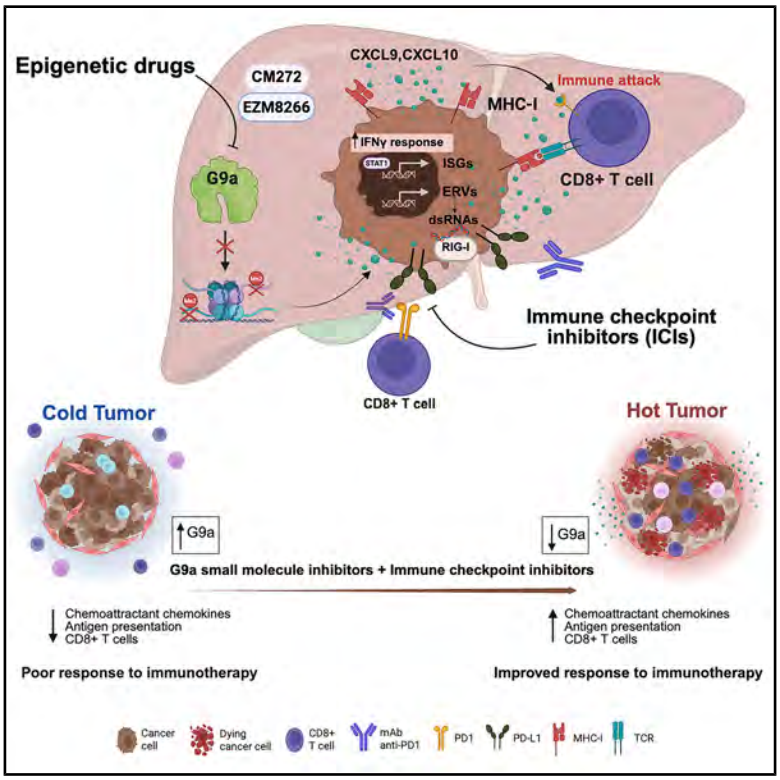

Highlights

- G9a expression inversely correlates with ICI-response signatures in HCC
- G9a inhibition enhances IFN-γ response and viral mimicry in HCC cells
- G9a targeting reshapes the TME toward an immunostimulatory state
- G9a inhibition synergizes with anti-PD1 in aggressive HCC models

Authors

Elena Adan-Villaescusa, Borja Castello-Uribe, Iker Uriarte, ..., Veronica Gibaja, Matias A. Avila, Maite G. Fernandez-Barrena

Correspondence

magarfer@unav.es

In brief

High G9a expression associates with immune exclusion and poor immunotherapy-response signatures in hepatocellular carcinoma. Adan-Villaescusa et al. demonstrate that G9a inhibition reprograms tumor cells through interferon sensitization and viral mimicry, restoring antitumor immunity. Combining G9a inhibitors with anti-PD1 overcomes resistance and drives durable antitumor immunity in preclinical HCC models.

Adan-Villaescusa et al., 2026, Cell Reports Medicine 7, 102717
April 21, 2026
https://doi.org/10.1016/j.xcrm.2026.102717

CellPress

Cell Reports Medicine

CellPress
OPEN ACCESS

Article

Histone methyl-transferase G9a inhibition boosts the efficacy of immune checkpoint inhibitors in experimental hepatocellular carcinoma

Elena Adan-Villaescusa,[1] Borja Castello-Uribe,[1] Iker Uriarte,[1,2] Eva Santamaria,[2,3] Roberto Barbero,[1,2] Miriam Belzunce,[1] Amaya López-Pascual,[1,4] Maria Ujue Latasa,[1] Jasmin Elurbide,[1,2] Emiliana Valbuena-Goiricelaya,[1] Agavni Mesropian,[5,6] Guillem Cano-Segarra,[5,6] Ana Hernández de Sande,[5] Lorenzo Nevi,[7] Simone Carotti,[7] Umberto Vespasiani-Gentilucci,[8] Felipe Prosper,[4,9,10] Antonio Pineda-Lucena,[11] Bruno Sangro,[2,4,12] Josepmaria Argemi,[2,3,4,12] Pedro Berraondo,[4,10,13] Pablo Sarobe,[2,4,13] Albert Gris-Oliver,[5,6] Roser Pinyol,[5,6] Josep M. Llovet,[5,6,14,15] Maria Arechederra,[1,2,4] Carmen Berasain,[1,2] Alexis Cocozaki,[16] Veronica Gibaja,[16] Matias A. Avila,[1,2,4,17] and Maite G. Fernandez-Barrena[1,2,4,17,18,*]

[1]Hepatology Laboratory, Solid Tumors Program, CIMA, CCUN, University of Navarra, Pamplona, Spain
[2]CIBERehd, Instituto de Salud Carlos III, Madrid, Spain
[3]RNA Biology and Therapy Program, CIMA, CCUN, University of Navarra, Pamplona, Spain
[4]Instituto de Investigaciones Sanitarias de Navarra IdiSNA, Pamplona, Spain
[5]Liver Cancer Translational Research Group, Institut d'Investigacions Biomèdiques August Pi i Sunyer (IDIBAPS), Hospital Clínic, Universitat de Barcelona, Barcelona, Catalonia, Spain
[6]Facultat de Medicina i Ciències de la Salut, Universitat de Barcelona, Barcelona, Catalonia, Spain
[7]Microscopic and Ultrastructural Anatomy Research Unit, Department of Medicine and Surgery, Università Campus Bio-Medico di Roma, Rome, Italy
[8]Unità di Epatologia, Università Campus Biomedico di Roma, Rome, Italy
[9]Hemato-Oncology Program, CIMA, CCUN, University of Navarra, Pamplona, Spain
[10]CIBERonc, Instituto de Salud Carlos III, Madrid, Spain
[11]Molecular Therapeutics Program, CIMA, CCUN, University of Navarra, Pamplona, Spain
[12]Hepatology Unit, CCUN, Navarra University Clinic, Pamplona, Spain
[13]Immunology and Immunotherapy Program, CIMA, CCUN, University of Navarra, Pamplona, Spain
[14]Mount Sinai Liver Cancer Program (Divisions of Liver Diseases, Department of Hematology/Oncology, Department of Medicine), Tisch Cancer Institute, Icahn School of Medicine at Mount Sinai, New York, NY USA
[15]Institució Catalana de Recerca i Estudis Avançats (ICREA), Barcelona, Catalonia, Spain
[16]Ipsen Biopharmaceuticals, Cambridge, MA, USA
[17]Senior author
[18]Lead contact
*Correspondence: magarfer@unav.es
https://doi.org/10.1016/j.xcrm.2026.102717

SUMMARY

Immune checkpoint inhibitors (ICIs) transform cancer therapy, but their efficacy in hepatocellular carcinoma (HCC) remains limited due to tumor-intrinsic immune evasion. We investigate the epigenetic regulator G9a (EHMT2) as a driver of immune resistance and evaluate pharmacologic inhibition as a therapeutic strategy. G9a expression is analyzed across human HCC cohorts and correlated with transcriptomic signatures predictive of ICI response. Using human and murine HCC cell lines and immunocompetent mouse models, we assess the antitumor effects of two G9a inhibitors, CM272 and EZM8266, combined with anti-PD1 therapy. Elevated G9a expression inversely correlates with immune-related signatures of ICI responsiveness. G9a inhibition restores interferon gamma (IFN-γ) signaling, increases major histocompatibility complex (MHC) class I expression, enhances CXCL10-mediated T cell recruitment, and induces viral mimicry via derepression of endogenous retroviral elements and cytosolic double-stranded RNA (dsRNA) accumulation. *In vivo*, G9a inhibition synergizes with anti-PD1 therapy, suppresses tumor growth, and enhances $CD8^+$ T cell infiltration. These findings support combining G9a inhibitors with immunotherapy in HCC.

INTRODUCTION

Hepatocellular carcinoma (HCC), the predominant form of primary liver malignancy, ranks among the most prevalent and lethal cancers globally, with an incidence that continues to rise.[1] HCC typically arises in the context of chronic hepatic injury and sustained inflammation, most frequently due to hepatitis B or C viral infections, alcohol-associated liver

Please cite this article in press as: Adan-Villaescusa et al., Histone methyl-transferase G9a inhibition boosts the efficacy of immune checkpoint inhibitors in experimental hepatocellular carcinoma, Cell Reports Medicine (2026), https://doi.org/10.1016/j.xcrm.2026.102717

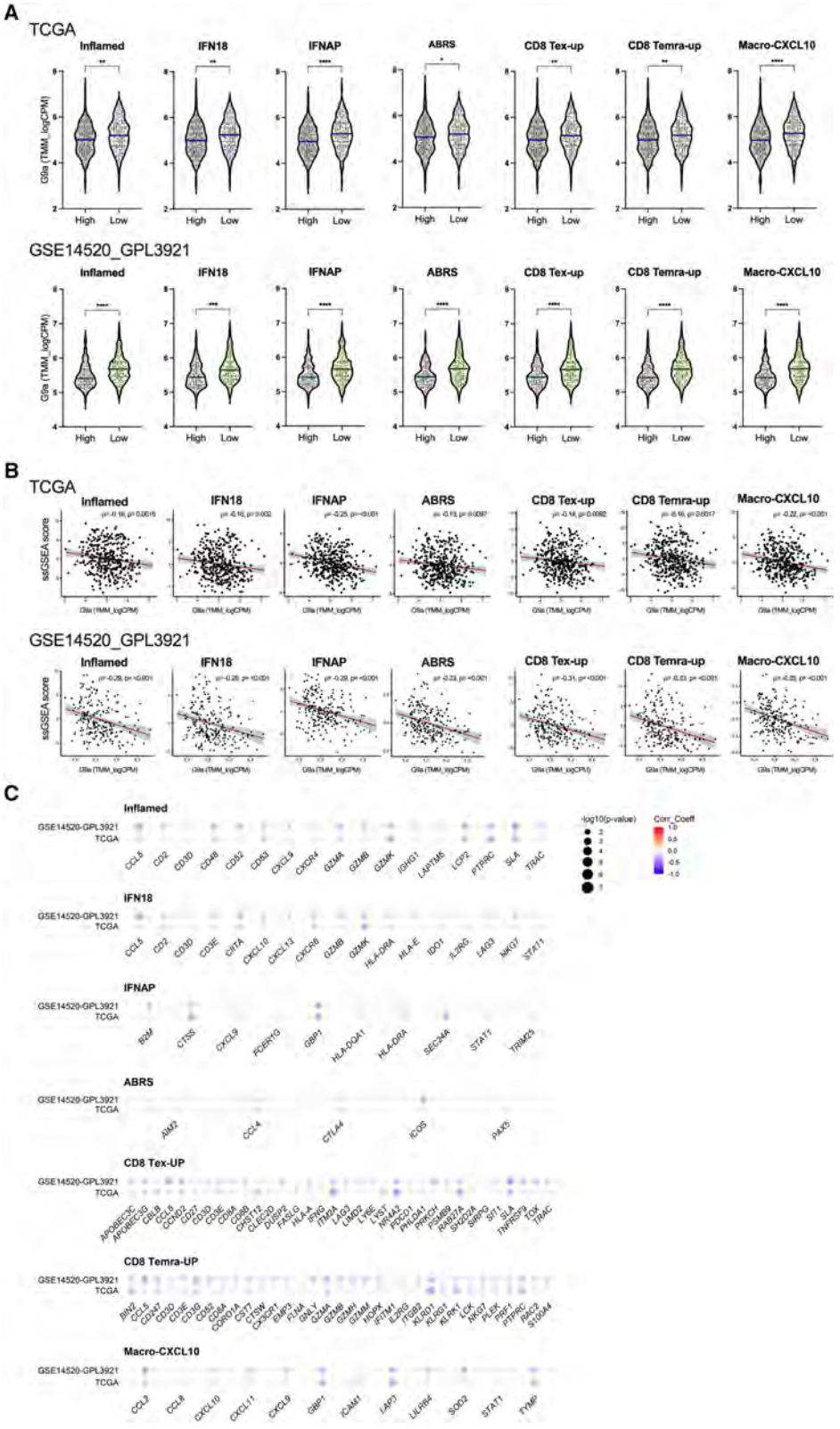

(legend on next page)

disease, and increasingly due to metabolic-dysfunction-associated steatotic liver disease (MASLD).[2] Although various treatment modalities exist, including surgical resection, liver transplantation, and locoregional therapies, clinical outcomes remain suboptimal, particularly in patients presenting with advanced disease stages, for whom systemic therapy constitutes the primary therapeutic avenue. In recent years, immunotherapeutic strategies have markedly expanded the therapeutic landscape for HCC, particularly immune checkpoint inhibitors (ICIs) targeting the PD1/PD-L1 and CTLA-4 axes. Notably, the combination of atezolizumab (an anti-PD-L1 monoclonal antibody) with bevacizumab (an anti-VEGF-A antibody) has demonstrated superior efficacy over sorafenib in advanced HCC, establishing a new first-line standard with a median overall survival of 19 months.[3] Furthermore, ICIs are actively being investigated in neoadjuvant and adjuvant contexts for early-stage disease, often in conjunction with surgery or local therapies.[4] Nevertheless, a substantial proportion of patients exhibit intrinsic resistance to ICIs, with only approximately 30% demonstrating objective clinical responses. Even among initial responders, many ultimately develop acquired resistance, limiting the durability of therapeutic benefit.[5] Thus, elucidating the mechanisms underlying immune evasion and identifying predictive biomarkers to guide patient stratification represent critical steps toward optimizing therapeutic efficacy in advanced HCC.

Various mechanisms have been implicated in both primary and acquired resistance, with increasing focus on the tumor microenvironment (TME), including immunosuppressive cell populations such as tumor-associated macrophages (TAMs), myeloid-derived suppressor cells (MDSCs), regulatory T cells (Tregs), inflammatory phenotypes, and T cell exhaustion.[6] Tumor cells further evade immune surveillance and cytolytic activity through complex genetic and epigenetic alterations,[7] which not only foster immune suppression but also interact with host-related factors such as diet, metabolism, and the gut microbiota,[8] ultimately contributing to immune resistance.

Epigenetic plasticity, including mechanisms such as DNA methylation, histone modification, and chromatin remodeling, plays a pivotal role in hepatocarcinogenesis, being strongly associated with tumor initiation, progression, and metastasis.[9–12] Importantly, emerging preclinical evidence suggests that specific epigenetic changes may modulate tumor-TME interactions and influence antitumor immune responses.[13] Although limited, emerging studies in murine HCC models have demonstrated that certain epigenetic regulators can affect tumor immune evasion and therapeutic resistance.[14] Consequently, pharmacological targeting of epigenetic regulators is being explored as a promising strategy to enhance the immunogenicity of HCC and improve ICI responsiveness.[15]

In this context, G9a (also known as EHMT2), a histone methyltransferase responsible for catalyzing mono- and dimethylation of histone H3 at lysine 9 (H3K9), is overexpressed in HCC and has been shown to orchestrate key oncogenic processes such as cell proliferation, survival, hypoxic adaptation, and metastasis.[16,17] Inhibition of G9a activity exerts potent antitumor effects in clinically relevant *in vitro* and *in vivo* HCC models, not only restoring tumor cell differentiation but also mitigating the pro-oncogenic influence of the fibrotic stroma that dominates the HCC TME.[16,18]

In the present study, we demonstrate that elevated G9a expression in HCC patients is inversely correlated with transcriptional signatures previously associated with favorable responses to ICI-based therapies. We subsequently examined the efficacy of two selective G9a inhibitors, our tool compound CM272[16,18–20] and the more clinically advanced molecule EZM8266,[21] in *in vitro* and *in vivo* HCC models. We observed how G9a blockade reinstated several key steps of the cancer-immunity cycle, including the upregulation of endogenous retroviruses (ERVs) and the reactivation of immune signaling pathways and chemokines in tumoral cells that promote T cell infiltration. When combined with anti-PD1 therapy, both inhibitors significantly suppressed tumor progression, in part by enhancing $CD8^+$ T cell recruitment and reshaping the TME toward a state permissive for effective antitumor immunity. These findings unveil a mechanistically grounded therapeutic combination capable of augmenting antitumor immunity and improving the efficacy of immunotherapy in HCC.

RESULTS

G9a expression negatively correlates with prognostic molecular signatures of ICI response in HCC patients

To explore whether expression of the histone methyltransferase G9a may influence response to ICIs in HCC, we first evaluated G9a transcript levels across The Cancer Genome Atlas (TCGA) HCC dataset and four additional independent HCC cohorts. Across all datasets analyzed, G9a expression demonstrated a consistent and statistically significant negative correlation with multiple gene signatures predictive of ICI response, including the Inflamed,[22] IFNAP,[23] IFN18,[24] and ABRS signatures.[25] When HCC patients are stratified according to the score of each predictive gene signature, those with lower signature scores, indicative of a poorer likelihood of response to immunotherapy, consistently exhibit higher levels of G9a expression (Figures 1A and S1A). Interestingly, a recent study employing single-cell RNA sequencing (scRNA-seq) of advanced HCC specimens identified 21 distinct cell-type-specific gene signatures.[26] The potential utility of these signatures as predictive biomarkers of response to atezolizumab and bevacizumab

Figure 1. G9a expression in HCC tissues is associated with gene signatures predictive of immune-based therapy response

(A) G9a expression in patients from the TCGA and GSE14520_GLP3921 HCC gene expression datasets stratified according to the score of the indicated predictive signatures.

(B) Spearman correlation plots showing the inverse association between G9a gene expression and the indicated signatures, as quantified by ssGSEA scores. Correlation coefficients (Spearman's ρ) and corresponding p values are indicated in each plot.

(C) Correlation between G9a expression and that of the different genes that constitute the indicated gene signatures in the TCGA and GSE14520_GLP3921 HCC gene expression datasets. $^{**}p < 0.01$, $^{***}p < 0.001$, $^{****}p < 0.0001$.

Please cite this article in press as: Adan-Villaescusa et al., Histone methyl-transferase G9a inhibition boosts the efficacy of immune checkpoint inhibitors in experimental hepatocellular carcinoma, Cell Reports Medicine (2026), https://doi.org/10.1016/j.xcrm.2026.102717

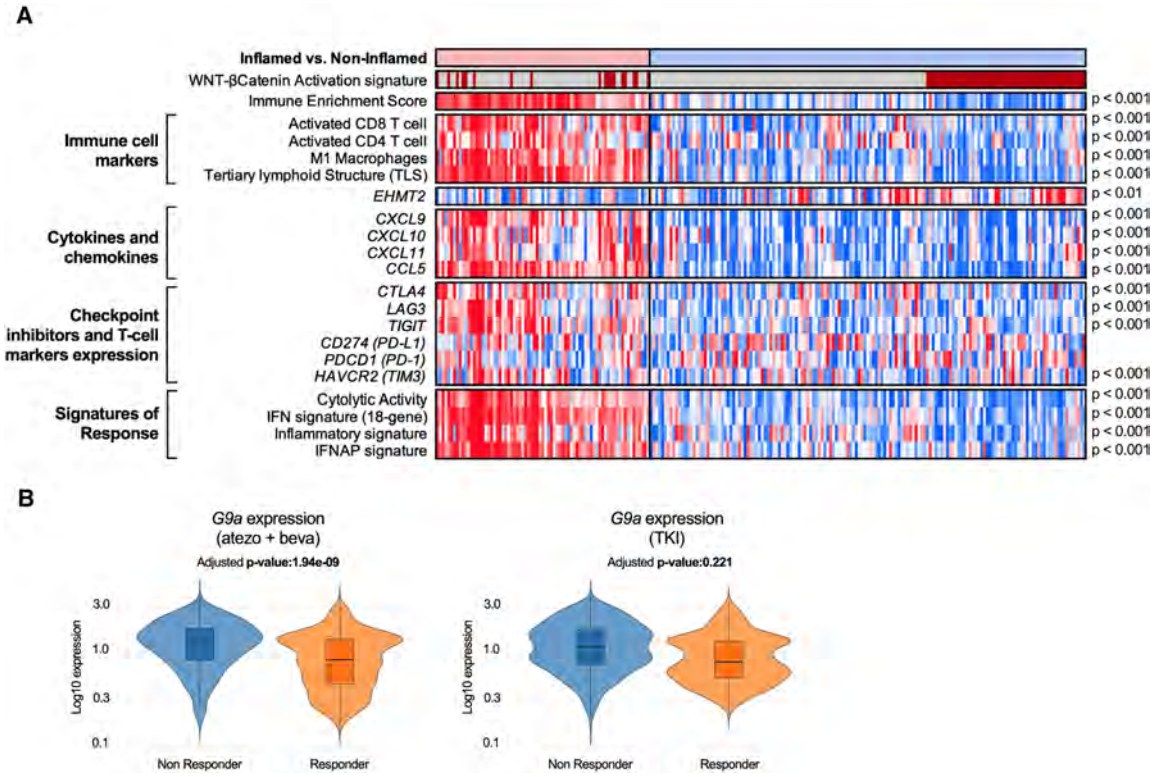

Figure 2. Association of G9a expression with therapy resistance

(A) Heatmap representation of the main molecular and immune features of the immune inflamed profile, related to the expression of G9a in HCC patients (n = 228). The gene signatures used for this figure can be found in Table S1. Statistical analysis: Student's t test for continuous variables.

(B) *G9a* expression per cell treated with atezo+beva (left) and *G9a* expression per cell treated with TKI, respectively. Non-responders in blue and responders in orange.

(atezo+bev) therapy was evaluated using bulk transcriptomic data from pretreatment advanced HCC samples. Different molecular subtypes of responders were delineated, one subgroup being characterized by the combined intratumoral presence of two $CD8^+$ effector T cell subtypes and $CXCL10^+$ macrophages, representing an immune-rich TME.[27] Notably, when applying these refined response-specific signatures across the same independent cohorts, G9a expression again showed a significant inverse correlation, further supporting the notion that patients with higher G9a expression levels consistently exhibit lower predictive signature scores (Figures 1B and S1B). We confirmed, both in the TCGA dataset and across other four independent HCC cohorts analyzed, how G9a expression exhibits in most of the cases a statistically significant negative correlation with multiple individual genes comprising each of the evaluated predictive signatures (Figures 1C and S1C). Finally, we analyzed an in-house HCC cohort comprising another 228 HCC patients. In this cohort, we also observed how G9a expression was inversely correlated with the HCC inflamed class,[22] with gene signatures predictive of ICI response,[23,24,28] immune cell markers (activated CD8,[29] M1 macrophages,[30] and tertiary lymphoid structures [TLSs][31]), and individually with the expression of cytokines, chemokines (*CXCL9*, *CXCL10*, *CCL11*, and *CCL5*), checkpoint inhibitors, and T cell markers (*CTLA4*, *LAG3*, *TIGIT*, and *TIM3*). Interestingly, G9a showed a strong positive correlation with Wnt-β catenin signaling,[32] previously related to immune cold tumors and ICI mono-therapy refractoriness[33] (Figure 2A). Lastly, we examined our recently published scRNA-seq dataset[26] comprising advanced HCC patients treated with the combination of atezo+bev, as well as a comparator cohort treated with tyrosine kinase inhibitors (TKIs). The *G9a* expression analysis at single-cell resolution showed how cells derived from non-responding patients exhibited significantly higher expression than those from responding patients (Wilcoxon test, $p = 1.94 \times 10^{-9}$). Notably, this association between high *G9a* expression and treatment resistance was specific to the immunotherapy cohort, as it was not observed in patients treated with TKI ($p = 0.221$) (Figure 2B). Collectively, these data implicate G9a as a potential negative regulator of antitumor immune responses in HCC and suggest its involvement in limiting patient responsiveness to ICI-based therapies.

G9a inhibition enhances the immunogenicity of HCC cells

To explore the tumor-intrinsic regulatory mechanism of G9a on immunity, RNA-seq analyses were performed in NM53 cells, a murine HCC cell line, treated with our selective epigenetic inhibitor CM272 in the absence or presence of interferon gamma (IFN-γ). We observed multiple changes in gene expression in NM53 cells in both conditions (Figure 3A). Consistently,

Please cite this article in press as: Adan-Villaescusa et al., Histone methyl-transferase G9a inhibition boosts the efficacy of immune checkpoint inhibitors in experimental hepatocellular carcinoma, Cell Reports Medicine (2026), https://doi.org/10.1016/j.xcrm.2026.102717

CellPress
OPEN ACCESS

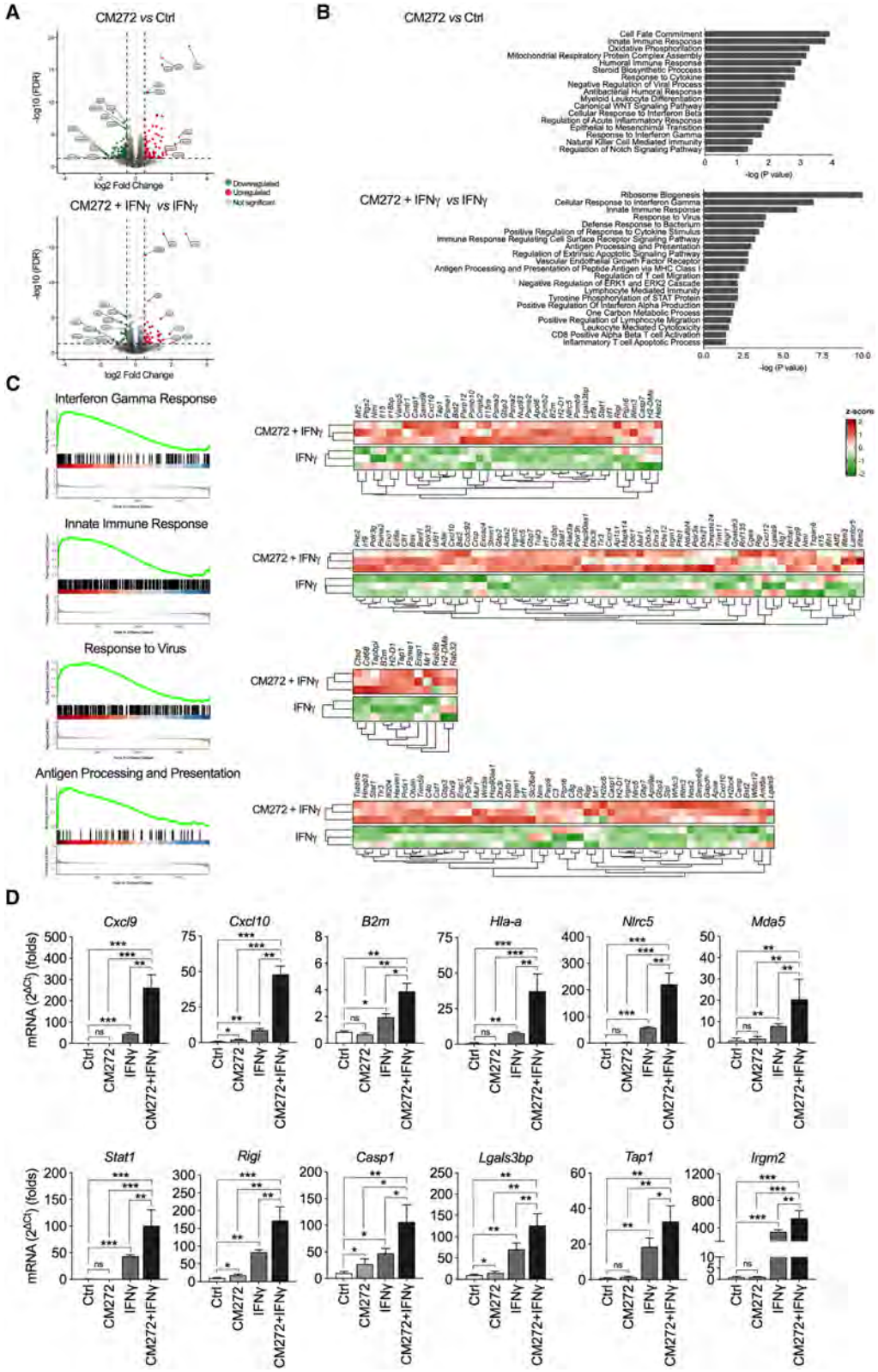

(legend on next page)

differentially expressed genes were involved in biological functions previously associated with the inhibition of G9a activity in HCC, such as oxidative phosphorylation and mitochondrial activity.[16] In addition, we identified genes involved in numerous biological processes related to immune pathways, including responses to cytokines or interferon (Figures 3B and S2A). Gene set enrichment analysis (GSEA) of differentially expressed genes highlighted various functional categories such as IFN-γ response (*Stat1* and *Cxcl10*), innate immune response (*Tap1* and *Psme1*), response to virus (*Irgm2*, *Cxcr4*, and *Cgas*), and antigen processing and presentation (*B2m*, *Tap1*, and *Psme1*) signaling pathways that were significantly enriched in CM272-treated cells. Interestingly, all these pathways were overrepresented in NM53 cells concomitantly stimulated with IFN-γ and CM272 (Figure 3C). To validate the abovementioned results, a second murine HCC cell line, PM299L,[33] was treated with CM272 in the presence or absence of IFN-γ. RT-qPCR analysis of the expression of key selected genes confirmed the effects of G9s inhibition on the response of HCC cells to IFN-γ (Figure 3D). Importantly, similar results were found in different human HCC cell lines (Figures S2B and S2C). In summary, these findings support the notion that G9a is involved in the repression of IFN-γ-responsive genes in human and mouse HCC cells.

Pharmacological inhibition of G9a with EZM8266 displays antitumoral properties in HCC

Because CM272 is a well-characterized dual inhibitor of G9a, but also of the epigenetic effector DNMT1, we sought to specifically delineate the contribution of G9a to the observed phenotypes by using another highly selective G9a inhibitor. To this end, we evaluated EZM8266, an orally available compound developed by Epizyme-Ipsen with favorable pharmacokinetic and pharmacodynamic properties.[21] To first evaluate the potential antitumor properties of this compound in the context of HCC, we conducted colony formation, anchorage-independent growth, and transwell assays in different human HCC cell lines. EZM8266 treatment markedly decreased colony formation, cell migration, and cell invasion in all cell lines tested (Figures 4A–4D). To gain insight into the mechanisms of the antitumoral effects of EZM8266, we performed RNA-seq analyses in a human HCC cell line. We detected 1,069 upregulated and 1,120 downregulated genes compared with controls ($p < 0.01$). Gene ontology (GO) functional classification of differentially expressed genes identified general categories linked to the regulation of diverse functions already associated with G9a activity, such as double-stranded DNA damage repair, autophagy, or L-serine metabolic processes.[16,34–37] Similarly, as observed in mouse HCC cells, G9a inhibition significantly increased the expression of many genes involved in innate immune response, interferon response, or processes such as double-stranded RNA (dsRNA) processing related to immunity (Figures 4F and 4G). Subsequently, we treated the murine HCC cell PM299L with EZM8266 in the absence or presence of IFN-γ (Figure 4H). We observed virtually the same changes as previously seen with CM272 treatment under both conditions. These results were also confirmed in mouse NM53 and human HCC cells (Figure S3).

Next, we examined the *in vivo* antitumoral properties of EZM8266 in a mouse model of orthotopic liver tumor growth. PM299L cells were subcutaneously injected in mice and after 4 weeks tumors were retrieved, cut into 1–2 mm^3 cubes and implanted into the left liver lobes of two groups of mice that were subsequently treated with EZM8266 or vehicle. We found that tumor growth was significantly reduced, and consistently tumor weights at the end of treatments were also significantly lower (Figure 4I). Immunohistochemical analysis revealed increased infiltration of $CD8^+$ T cells in the smaller tumors observed in EZM8266-treated mice compared with controls. Similarly, $CD4^+$ T cell immunostaining showed higher intratumoral levels following EZM8266 treatment (Figure 4J).

G9a inhibition enhances tumor cell immunogenicity and promotes immune-stimulatory pathways in HCC cells

According to our transcriptomic analyses in NM53 cells treated with CM272 and IFN-γ, G9a inhibition seems to impinge on different mechanisms related to the activation of immunogenic pathways in HCC cells. In agreement with these findings, we observed that CM272 and IFN-γ combination strongly enhanced CXCL10 release in both mouse and human HCC cells (Figures 5A and S4A). Furthermore, we also demonstrated that G9a inhibition led to a significant increase in cell surface expression of the MHC class I complex proteins. We validated these findings in cells treated with EZM8266 (Figures 5B and S4B). To gain more direct evidence on the role of G9a in the regulation of the expression of immune-response-related genes, we performed ChIP analyses of the repressive G9a-mediated H3K9me2 mark in the promoter regions of relevant genes, such as *CXCL10* and different MHC class I genes, such as *HLA-A*, *HLA-B*, and *HLA-C*. As shown in Figures 5C and S4D, the H3K9me2 mark, which was enriched in these promoters, was significantly suppressed in HuH7 cells upon CM272 treatment. Moreover, CM272 enhanced the mild inhibitory effect that IFN-γ has on this repressive epigenetic mark (Figure 5C). These effects were reproduced in HuH7 cells treated with EZM8266 (Figures S4C and S4D).

Figure 3. G9a inhibition enhances the immunogenicity of HCC cells

(A) Volcano plots representing all the genes with significant differential expression ($p < 0.05$) in NM53 murine HCC cells treated with CM272 (400 nM for 48 h, upper panel) vs. control (Ctrl) cells or with CM272 (400 nM) for 24 h and then with IFN-γ (75 U/mL) for another 24 h vs. IFN-γ alone (75 U/mL for 48 h, lower panel), as analyzed by RNA-seq.

(B) Most relevant categories of differentially expressed genes identified by Gene Ontology Biological Process (GO-BP) functional classification in NM53 cells treated as indicated before.

(C) GSEA analysis of specific categories including heatmaps with a list of genes modulated by IFN-γ vs. IFN-γ plus CM272 selected from the RNA-seq data.

(D) Validation of the effects of CM272, IFN-γ, and their combination, as indicated above, on the expression of selected genes identified in the RNA-seq analyses in the murine HCC cell line PM299L ($n = 3$). Data are represented as mean ± SEM. $^*p < 0.05$, $^{**}p < 0.01$, $^{***}p < 0.001$. All the replicates represent biological replicates.

Please cite this article in press as: Adan-Villaescusa et al., Histone methyl-transferase G9a inhibition boosts the efficacy of immune checkpoint inhibitors in experimental hepatocellular carcinoma, Cell Reports Medicine (2026), https://doi.org/10.1016/j.xcrm.2026.102717

CellPress
OPEN ACCESS

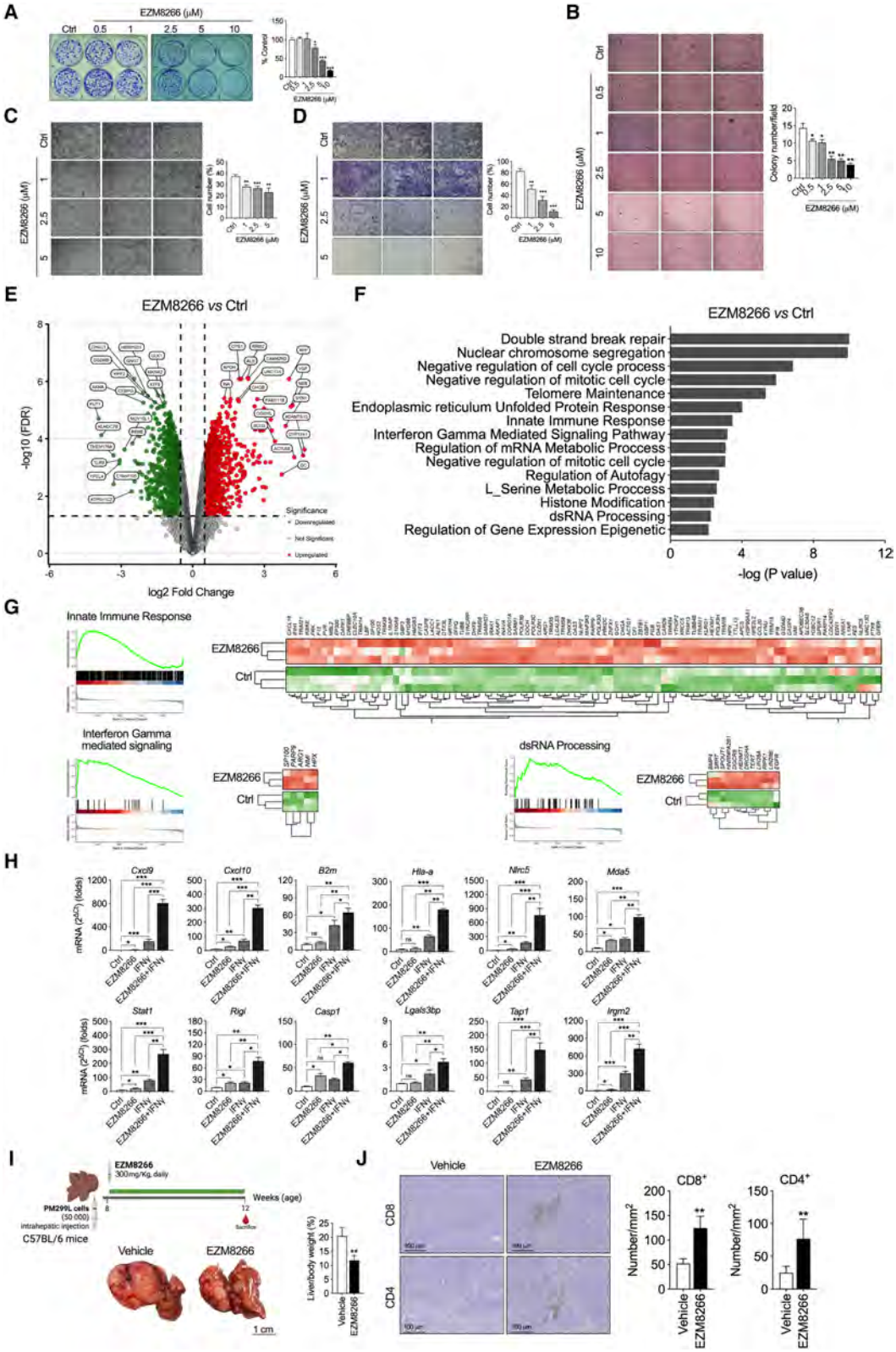

(legend on next page)

Please cite this article in press as: Adan-Villaescusa et al., Histone methyl-transferase G9a inhibition boosts the efficacy of immune checkpoint inhibitors in experimental hepatocellular carcinoma, Cell Reports Medicine (2026), https://doi.org/10.1016/j.xcrm.2026.102717

Transposable elements (TEs) and endogenous retroviral sequences (ERVs) are DNA segments repressed through various epigenetic mechanisms, including those mediated by histone methyltransferases such as SETDB1.[38] When these epigenetic modifications are removed, TEs and ERVs are transcribed, generating immunostimulatory dsRNAs.[39] This response, termed viral mimicry, has been observed in the context of the inhibition of different epigenetic effectors, including DNA and histone-methyltransferases, in other epithelial cancers.[40,41] These host-derived dsRNAs mimicking viral dsRNA are detected by intracellular sensors such as RIG-I and MDA5, triggering an interferon response.[39] Interestingly, *RIGI* was one of the most upregulated genes in HCC cells treated with G9a inhibitors plus IFN-γ (Figure 3D). We observed that the inhibition of G9a resulted in the upregulation of the expression of TE loci in NM53 mouse HCC cells and that G9a targeting potentiated the response to IFN-γ. We observed induction of several endogenous retroviruses (ERVK, ERV1, and ERVL) and LINE families, including L1, L2, or hAT transposable elements (Figure 5D). Consistent with a direct epigenetic mechanism, ChIP-qPCR analyses demonstrated a marked reduction of the repressive H3K9me2 mark at the promoters of selected ERVs, such as *HERV* or *MLT1N2*,[40] upon treatment with the two epigenetic inhibitors (Figure S4E). Accordingly, immunofluorescence analyses revealed a significant accumulation of intracellular dsRNA in both murine and human HCC cells following G9a inhibition, particularly in the presence of IFN-γ (Figures 5E and S4F). To determine whether viral mimicry contributes to the transcriptional response driven by G9a inhibition, we silenced the dsRNA sensor *RIGI* and assessed IFN-γ-induced gene expression following pharmacological (Figures S4G and S4H) or genetical (Figure S4I) G9a targeting. Although *RIGI* depletion partially attenuated the induction of target chemokines such as *CXCL10*, this effect was not fully abolished, as chemokine expression remained significantly increased following G9a inhibition even in the absence of *RIGI* (Figures S4G–S4I), indicating the coexistence of viral mimicry-dependent and -independent mechanisms. Collectively, these findings indicate that specific G9a inhibition simultaneously triggers different immunostimulant mechanisms in HCC cells potentiating the response to IFN-γ.

EZM8266 increases the efficacy of ICIs in an orthotopic HCC mouse model

In view of these compelling observations, we next investigated the effects of G9a inhibition on the therapeutic response to PD1 blockade in an orthotopic mouse HCC model (Figure 6A). While EZM8266 monotherapy showed a significative, albeit limited effect, tumor growth was substantially abrogated when EZM8266 treatment was combined with anti-PD1 antibodies (Figure 6B). Importantly, this therapeutic response was not accompanied by any observable unwanted effects, including weight loss (Figure S5A). Moreover, the combination therapy significantly decreased the serum alanine transaminase, aspartate transaminase, and lactate dehydrogenase levels to those found in age-matched normal mice (Figure 6C). Immunohistochemical analyses revealed a significant reduction of the repressive H3K9me2 mark in tumors from EZM8266-treated mice, while total G9a protein levels remained unchanged (Figures S5B and S5C). Immunostaining analyses showed that EZM8266 or anti-PD1 treatment induced $CD8^+$ T cell infiltration in tumoral areas, and this response was significantly increased in mice treated with EZM8266 in combination with anti-PD1 antibodies (Figure 6D). Similarly, an increase in $CD4^+$ T cells was observed in the group of mice treated with the combination, although it did not reach statistical significance. CXCL10 chemokine expression was significantly increased in tumor areas from animals treated with EZM8266 (Figure S5D). In parallel, quantitative PCR analyses of tumor tissues revealed elevated expression of MHC-class-I-related genes, including *H2-Q2* (the murine ortholog of HLA-A), as well as the retroelement *MERVL*[42] (Figure S6A). These results suggest that G9a inhibition triggers effective anti-tumor immunity mechanisms and provide a rationale for combining G9a inhibitors with ICIs to treat HCC.

G9a targeting with different tool compounds increases the efficacy of ICI in aggressive orthotopic and genetic HCC models

To further corroborate our findings, we next sought to confirm whether G9a inhibition with our other tool compound CM272, could enhance the efficacy of immune checkpoint blockade in a more aggressive orthotopic HCC setting subjected to post-hepatectomy inflammatory conditions. In this model, HCC cells were injected into one of the remaining liver lobes following

Figure 4. Antitumoral effects of the G9a-specific inhibitor EZM8266

(A) Colony formation assays performed in PLC/PRF/5 human HCC cells treated with the indicated concentrations of EZM8266 ($n = 3$).

(B) Anchorage-independent growth assay performed in PLC/PRF/5 cells treated with the indicated concentrations of EZM8266.

(C and D) Cell migration (C) and cell invasion (D) assays performed in HuH7 cells treated with the indicated concentrations of EZM8266 (48 h pretreatment and 24 h of transwell migration/invasion) ($n = 3$).

(E) Volcano plot representing all the genes with significant differential expression ($p < 0.05$) in PLC/PRF/5 HCC cells treated with EZM8266 (5 μM for 48 h) vs. control cells and most relevant categories of differentially expressed genes identified by Gene Ontology Biological Process (GO-BP) functional classification.

(F) GSEA analysis of specific categories including heatmaps with a list of genes modulated by EZM8266 selected from the RNA-seq data.

(G) Effect of EZM8266, IFN-γ, and their combination on the expression of selected genes in the murine HCC cell line PM299L ($n = 3$).

(H) Validation of the effects of EZM8266, IFN-γ, and their combination, as indicated above, on the expression of selected genes identified in the RNA-seq analyses in the murine HCC cell line PM299L ($n = 3$).

(I) Experimental protocol for the study of the antitumoral effects of EZM8266 in an orthotopic model of HCC. Representative images of tumors and tumor burden (liver index) in vehicle and EZM8266-treated mice ($n = 9$/group).

(J) Representative images showing the immunohistochemical detection of $CD4^+$ and $CD8^+$ T cells and quantification of tumor-infiltrating $CD8^+$ and $CD4^+$ T cells (yellow arrows) in vehicle- and EZM8266-treated mice. Scale bars, 100 μm, Data are represented as mean ± SEM. $^*p < 0.05$, $^{**}p < 0.01$, $^{***}p < 0.001$. All the replicates represent biological replicates.

Please cite this article in press as: Adan-Villaescusa et al., Histone methyl-transferase G9a inhibition boosts the efficacy of immune checkpoint inhibitors in experimental hepatocellular carcinoma, Cell Reports Medicine (2026), https://doi.org/10.1016/j.xcrm.2026.102717

CellPress
OPEN ACCESS

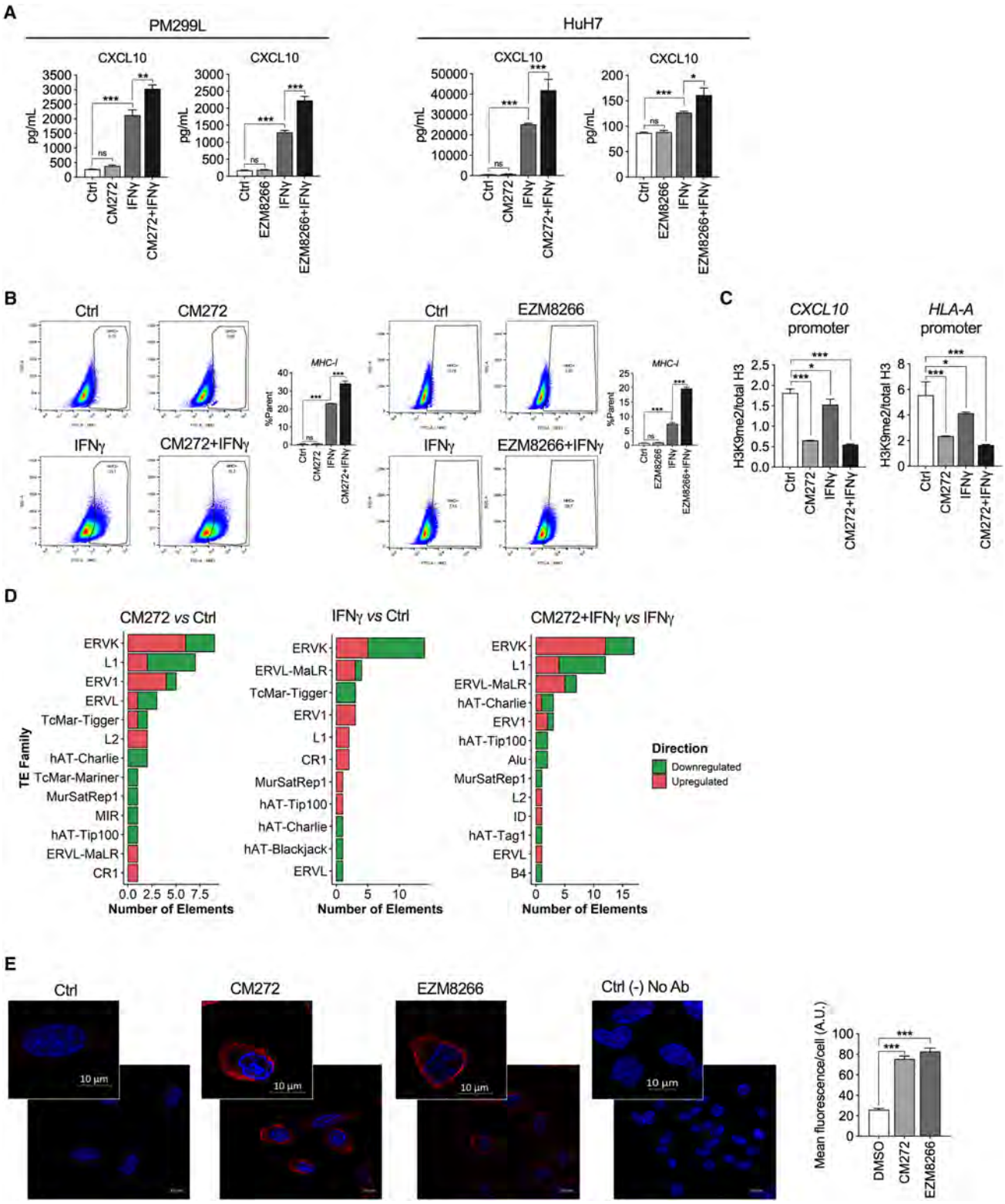

Figure 5. G9a inhibition potentiates the immunogenic effects of IFN-γ in HCC cells

(A) Effect of CM272 and EZM8266 on IFN-γ-triggered CXCL10 production in murine (PM299L) and human (HuH7) HCC cells. Cells were treated with CM272 for 48 h or with CM272 for 24 h and then with IFN-γ (75 U/mL) for another 24 h or with IFN-γ alone for 24 h. PM299L were treated with 400 nM, and HuH7 received 1 μM

(legend continued on next page)

partial liver resection (Figure 7A). Monotherapy with CM272 induced a moderate antitumor effect, and anti-PD1 antibody administration led to a noticeable reduction in tumor burden as well. Strikingly, the combination of CM272 and anti-PD1 therapy resulted in marked tumor regression (Figures 7B and 7C). In alignment with our previous observations using EZM8266, no adverse effects were detected in terms of body weight loss in CM272-treated animals (Figure S5E). Notably, a marked reduction in the repressive H3K9me2 mark was observed in tumors from CM272-treated mice (Figure S5F), while total G9a protein levels remained unchanged (Figure S5G). The combinatorial approach also reshaped the immune cell landscape within tumor tissues. Specifically, the proportion of tumor-infiltrating $CD8^+$ T cells was significantly increased in CM272-treated mice compared to controls, with further enhancement observed upon anti-PD1 co-treatment. Likewise, $CD4^+$ T cell infiltration was significantly elevated in the combination treatment group relative to controls (Figure 7E), as well as the CXCL10 expression (Figure S5H). The expression levels of genes such as *H2-Q2* or ERVs such as *MERVL* were also significantly increased in the combination group (Figure S6B). Moreover, flow-cytometry-based profiling of additional cellular populations within the TME revealed notable changes in myeloid cell subsets, especially in animals receiving the CM272 and anti-PD1 combination, consistent with a more immunologically active tumor milieu (Figure S6C). CM272 treatments increased dendritic cell frequencies and reduced MDSCs, with no major changes in monocytes or TAMs. Nevertheless, TAMs displayed increased expression of MHC class II and activation markers (CD86), together with reduced arginase 1 (Arg1) expression, indicative of a shift toward an inflammatory phenotype. Monocytes similarly showed increased activation marker expression and decreased Arg1 levels (Figure S6D).

Finally, we employed an alternative HCC model based on the hydrodynamic tail vein injections of transposon vectors expressing the oncogenes MYC (pT3-EF1a-MYC), activated βcatenin (CTNNB1-Δ90, which presents a deletion of the 90 first amino acids leading to constitutive activation), and a vector expressing SB13 transposase (CMV-SB13), which is required to integrate the transposon-based vectors into the hepatocyte genomic DNA. In this experimental HCC model, β-catenin activation promotes immune escape and resistance to anti-PD1.[33] In line with our previous observations, monotherapy with either CM272 or EZM8266 elicited a significant antitumor response, whereas treatment with anti-PD1 alone failed to confer therapeutic benefit. Notably, combining either G9a inhibitor with anti-PD1 resulted in a pronounced reduction in tumor burden (Figures S7A–S7C). Flow cytometric analysis of the TME revealed a remodeling of immune cell composition consistent again with a less immunosuppressive landscape. Combined G9a inhibition and anti-PD1 therapy increased the infiltration of $CD8^+$ and $CD4^+$ T lymphocytes, with a trend toward a decreased $CD4^+$:$CD8^+$ ratio. Importantly, $CD8^+$ T cells did not exhibit features of overt exhaustion, as LAG-3 expression was unaltered, and PD1 levels showed only a modest increase, consistent with T cell activation rather than terminal dysfunction. Effector memory subsets within both $CD4^+$ and $CD8^+$ compartments were preserved, further arguing against exhaustion-driven differentiation. Regulatory T cells were reduced across treatment groups and exhibited a tendency toward increased PD1 expression (Figure S7D). Collectively, these findings confirm how G9a inhibition potentiates the therapeutic efficacy of anti-PD1 in HCC, supporting its use as a promising combinatorial strategy across different scenarios.

DISCUSSION

Immunotherapy has revolutionized cancer treatment in the past decade, with ICIs becoming a cornerstone of therapy in various malignancies.[43] However, in HCC, the clinical benefit of ICIs remains limited to a subset of patients.[3] This underscores the pressing need to identify novel molecular targets and rational combination strategies to enhance immunotherapeutic efficacy in this setting. The inherent ability of HCC to escape immune surveillance presents a major challenge for the successful implementation of immunotherapy in clinical practice.[4] In this context, tumor cells exploit both genetic and epigenetic mechanisms to evade immune detection and destruction. Recent studies have highlighted the role of epigenetic regulators in modulating antitumor immunity, positioning them as attractive combinatorial partners for ICIs. Although relatively few studies have investigated this in HCC specifically, inhibitors targeting DNA methyltransferases (DNMTs), histone deacetylases (HDACs), the histone methyltransferase EZH2, or bromodomain and extra-terminal domain (BET) proteins have demonstrated the potential to enhance ICIs efficacy.[14] Nevertheless, a comprehensive preclinical validation remains necessary before these strategies can be clinically implemented. In the present study, we provide evidence that the histone methyltransferase G9a can play a significant role in modulating resistance to immunotherapy in HCC. Using an integrative approach that included the TCGA cohort, four independent HCC transcriptomic datasets,[44–46] and an in-house HCC cohort encompassing a total of 992 patients, we observed that high G9a expression inversely correlated with

of CM272 ($n = 3$). For EZM8266, cells were pretreated for 48 h with EZM8266 (5 mM) and then with IFN-γ (75 U/mL) for another 24 h, as indicated. CXCL10 protein levels were measured by ELISA in cells' conditioned media ($n = 3$).

(B) Effect of G9a inhibition with CM272 or EZM8266 on the expression of MHC class I complex protein (MHC-I) on the surface of PM299L cells. Cells were treated with IFN-γ and CM272 or EZM8266 as indicated in (A), and MHC-I levels were determined by FACS analysis ($n = 3$).

(C) ChIP analyses of H3K9me2 levels in the proximal promoter regions of *CXCL10* and *HLA-A* genes in HuH7 cells treated with IFN-γ (75 U/mL) and CM272 (400 nM), as indicated in (A) ($n = 3$).

(D) Evaluation of the expression of transposable elements (TEs) and endogenous retroviral sequences (ERVs) by RNA-seq in NM53 murine HCC cells treated with IFN-γ, CM272, and their combination as indicated in (A).

(E) Immunofluorescence analyses of dsRNA in PM299L HCC cells treated with CM272 (24 h) or EZM8266 (48 h). Representative images are shown. Scale bars, 10 μm. Right panel shows a control without primary antibody ($n = 3$). Data are represented as mean ± SEM. $^*p < 0.05$, $^{**}p < 0.01$, $^{***}p < 0.001$. All the replicates represent biological replicates.

Please cite this article in press as: Adan-Villaescusa et al., Histone methyl-transferase G9a inhibition boosts the efficacy of immune checkpoint inhibitors in experimental hepatocellular carcinoma, Cell Reports Medicine (2026), https://doi.org/10.1016/j.xcrm.2026.102717

CellPress
OPEN ACCESS

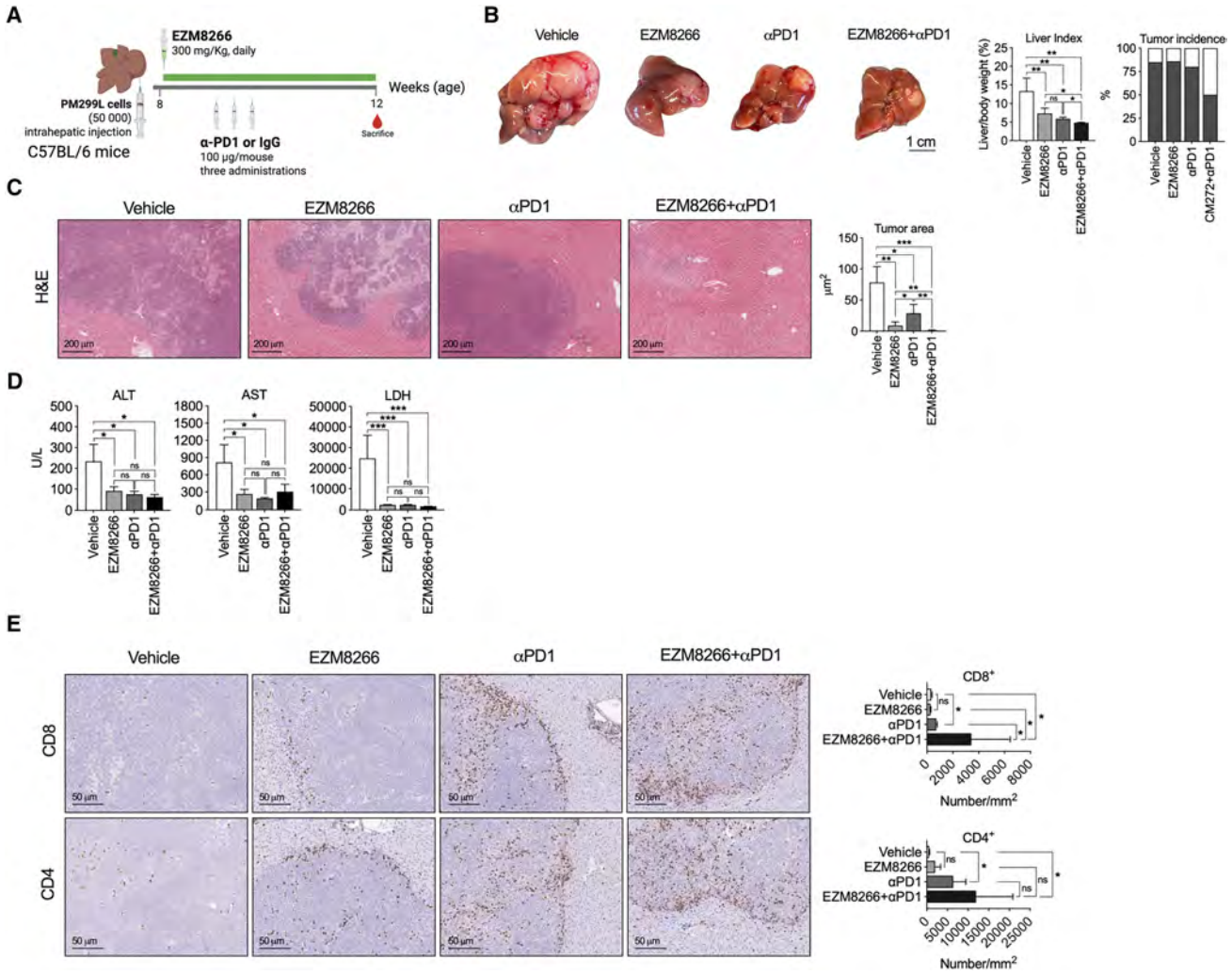

Figure 6. G9a inhibition with EZM8266 potentiates the *in vivo* antitumoral effect of ICI

(A) Experimental protocol for the study of the antitumoral effects of EZM8266 in combination with ICI in an HCC model developed by the orthotopic implantation of PM299L cells in immunocompetent mice.

(B) Representative images of tumors in the different groups of mice at the end of treatments. Scale bars, 1 cm. Quantitation of tumor burden (liver index) and tumor incidence is indicated (n = 10/group).

(C) Histological evaluation of tumor growth (tumor area) in the different treatment groups. Representative images of H&E-stained liver and tumor tissues are shown. Scale bars, 200 µm.

(D) Serum levels of ALT, AST, and LDH in the different groups of mice at the end of treatments.

(E) Representative images showing the immunohistochemical detection of $CD4^+$ and $CD8^+$ T cells and quantification of tumor-infiltrating $CD8^+$ and $CD4^+$ T cells in the different groups of mice at the end of treatments. Scale bars, 50 µm. Data are represented as mean ± SEM. $^*p < 0.05$, $^{**}p < 0.01$, $^{***}p < 0.001$. All the replicates represent biological replicates.

relevant gene expression signatures predictive of ICI response. We first assessed the relationship between G9a expression and established HCC molecular subclasses, including the Inflamed class[22] and the IFN18 signature.[24] In addition, we evaluated its association with a series of immune gene signatures known to distinguish responders from non-responders to ICIs, such as IFNAP,[23] ABRS,[25] and more recently developed single-cell-derived signatures including CD8-Tex, CD8-Temra, and Macro-CXCL10.[27] Strikingly, patients with low scores across these immune signatures consistently displayed elevated G9a expression, a pattern that was also observed in non-responders to atezolizumab plus bevacizumab therapy compared with patients who derived clinical benefit. These findings suggest that G9a overexpression may contribute to an immunosuppressive tumor microenvironment and impaired response to ICIs in HCC. Thus, targeting G9a could represent a strategy to restore immune surveillance and overcome resistance to immunotherapy in this neoplasia. Importantly, the role of G9a in modulating immune responses has been previously explored in preclinical models of several tumor types, such as melanoma[37] or bladder cancer[47] with promising results. Our study expands this growing body of evidence by demonstrating its clinical

Please cite this article in press as: Adan-Villaescusa et al., Histone methyl-transferase G9a inhibition boosts the efficacy of immune checkpoint inhibitors in experimental hepatocellular carcinoma, Cell Reports Medicine (2026), https://doi.org/10.1016/j.xcrm.2026.102717

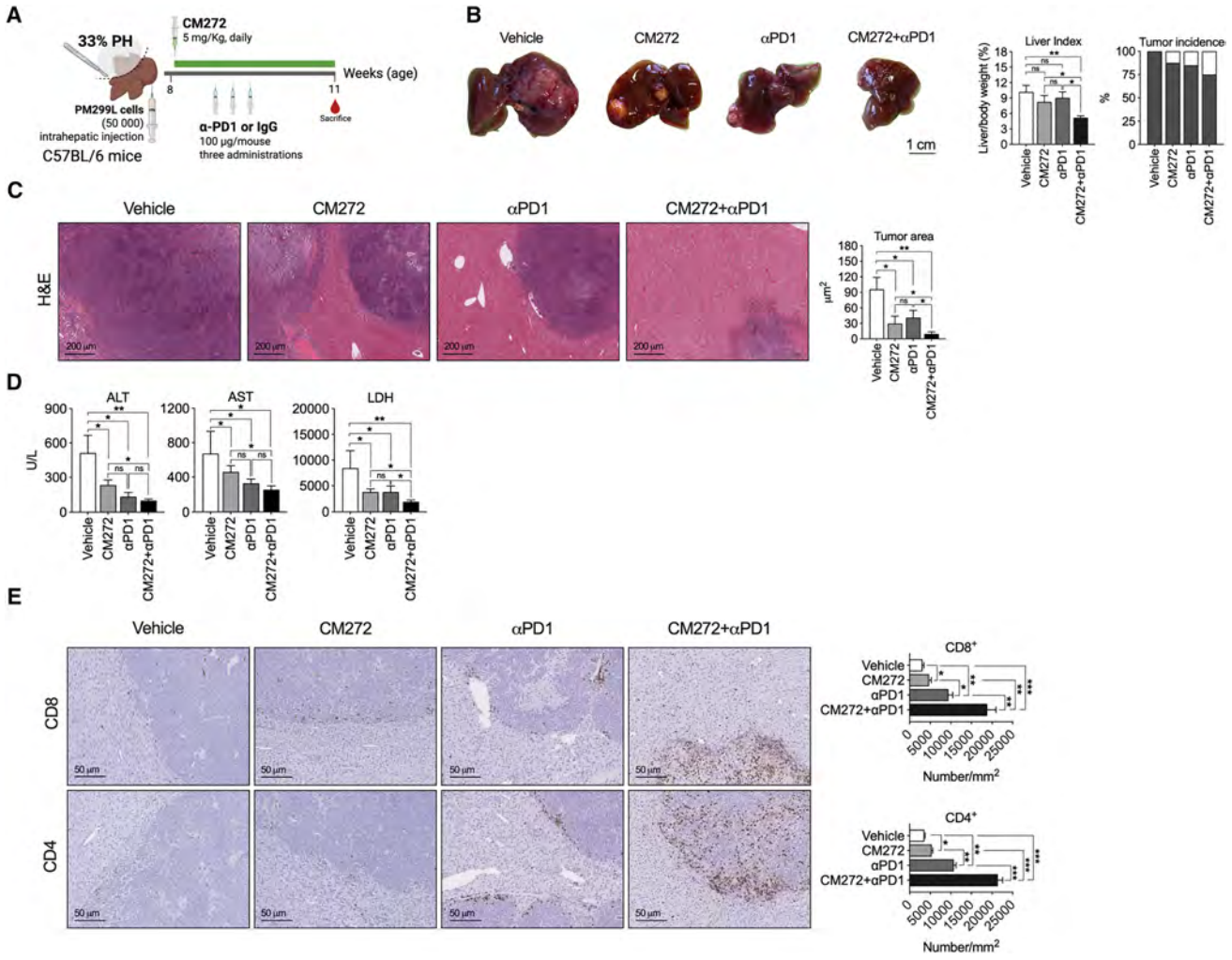

Figure 7. G9a inhibition with CM272 potentiates the *in vivo* antitumoral effect of ICI in an aggressive model of PH-stimulated HCC growth

(A) Experimental protocol for the study of the antitumoral effects of CM272 in combination with ICI in an HCC model developed by the orthotopic implantation of PM299L cells in immunocompetent mice and a concomitant partial hepatectomy (33% PH) (n = 10/group).

(B) Representative images of tumors in the different groups of mice at the end of treatments. Scale bars, 1 cm. Quantitation of tumor burden (liver index) and tumor incidence is indicated.

(C) Histological evaluation of tumor growth (tumor area) in the different treatment groups. Representative images of H&E-stained liver and tumor tissues are shown. Scale bars, 200 μm.

(D) Serum levels of ALT, AST, and LDH in the different groups of mice at the end of treatments.

(E) Representative images showing the immunohistochemical detection of CD4$^+$ and CD8$^+$ T cells and quantification of tumor-infiltrating CD8$^+$ and CD4$^+$ T cells in the different groups of mice at the end of treatments. Scale bars, 50 μm. Data are represented as mean ± SEM. $^*p < 0.05$, $^{**}p < 0.01$, $^{***}p < 0.001$.

relevance in patients with HCC. Interestingly, the role of G9a has been previously examined in the immune compartment as an epigenetic regulator influencing T cell cytotoxicity.[48] In a study utilizing engineered T cells targeting HCC, short-term inhibition of G9a enhanced T cell antitumor activity both *in vitro* and in an orthotopic mouse model. Specifically, G9a blockade increased granzyme expression without promoting terminal T cell differentiation or exhaustion and induced selective transcriptional and proteomic changes in genes involved in pro-inflammatory signaling, T cell activation, and cytotoxicity.[48] These findings are highly consistent with our observation that G9a expression in HCC patients inversely correlates with a wide range of immune-related genes implicated in these mentioned processes. These include genes involved in cytolytic activity (e.g., *GZMA*, *GZMB*, *GZMK*, *GZMH*, and *PRF1*), inflammation-initiation chemokines (*CXCL9*, *CXCL10*, *CXCL11*, *CCL2*, *CCL4*, and *CCL5*), T cell markers (*CD3D*, *CD3E*, *CD3G*, and *CD8A*), natural killer (NK) cell cytotoxicity (*NKG7*, *KLRD1*, and *KLRK1*), antigen presentation (*CIITA*, *HLA-DRA*, *B2M*, and *PTPRC*), as well as other immunomodulatory molecules such as *IFITM1*, *PRKCH*, and *GBP1*. Collectively, these data provide a compelling rationale for exploring the specific role of G9a in HCC tumor cells and for the development of innovative G9a-targeting agents as part of combination immunotherapy strategies in HCC.

Please cite this article in press as: Adan-Villaescusa et al., Histone methyl-transferase G9a inhibition boosts the efficacy of immune checkpoint inhibitors in experimental hepatocellular carcinoma, Cell Reports Medicine (2026), https://doi.org/10.1016/j.xcrm.2026.102717

Currently, a number of small-molecule inhibitors have been developed to target G9a with acceptable, though limited, therapeutic efficacy. However, most of them have not progressed to clinical trials due to suboptimal physicochemical and pharmacokinetic properties.[49] In the present work, we investigated the molecular consequences of G9a inhibition in murine HCC cells using two promising inhibitors: CM272, a selective, reversible chemical probe with previously demonstrated antitumor activity in HCC models,[16] and EZM8266, a highly selective G9a inhibitor in advanced stages of preclinical development.[21] Our data demonstrate that EZM8266 exerts potent antitumor effects in HCC. Functional assays revealed that EZM8266 significantly impaired HCC cell clonogenicity, migration, and invasiveness *in vitro*. Moreover, different experimental HCC models confirmed that *in vivo* administration of EZM8266 substantially reduced tumor growth in immunocompetent mice, with no signs of systemic toxicity and an excellent safety profile. Mechanistically, our data demonstrate that G9a inhibition in HCC tumor cells disrupts multiple layers of immune evasion by enhancing tumor cell immunogenicity and promoting immune-stimulatory pathways. Pharmacologic targeting of G9a using two structurally distinct inhibitors induced broad transcriptional reprogramming characterized by the activation of interferon signaling and other immune-associated pathways. In both murine and human HCC cells, G9a inhibition synergized with IFN-γ to enhance the transcription of immune effector genes, including those encoding chemokines such as CXCL10 and components of MHC class I, thereby promoting both lymphocyte recruitment and tumor cell visibility to cytotoxic immune cells. We confirmed a robust increase in IFN-γ-induced CXCL10 secretion upon treatment with either CM272 or EZM8266. In parallel, our flow cytometric analyses revealed significantly enhanced surface expression of MHC class I molecules on HCC cells, particularly under combination with IFN-γ stimulation, suggesting that G9a inhibition facilitates antigen presentation. Chromatin immunoprecipitation assays demonstrated a marked reduction of the repressive histone mark H3K9me2 at the promoters of *CXCL10*[50] and *MHC-I* genes,[51] indicating that G9a inhibition epigenetically primes chromatin for transcriptional activation. In addition to reprogramming immune-related gene expression, G9a inhibition consistently upregulated transcripts derived from TEs, particularly ERVs. This observation is in line with prior studies demonstrating that inhibition of epigenetic repressors such as DNMT1,[40] SETDB1,[52] or even G9a in other types of tumors[21,40] can derepress ERVs, leading to their transcriptional activation. These sequences, remnants of ancient viral integrations into the host genome, can trigger innate antiviral responses via the induction of dsRNA and the subsequent activation of viral defense pathways, a phenomenon termed "viral mimicry."[39] In our study, G9a inhibition induced a significant accumulation of immunostimulatory dsRNA in both mouse and human HCC cells, further supporting the engagement of viral mimicry as a key mechanism for enhancing tumor immunogenicity.

Collectively, these data establish that G9a inhibition not only reverses epigenetic silencing of immune-stimulatory genes and TEs but also fundamentally increases tumor immunogenicity. This mechanistic insight provided the rationale for combining G9a inhibitors with immune checkpoint blockade. Indeed, combinatorial treatment with either CM272 or EZM8266 and anti-PD1 antibodies led to near-complete regression of different experimental settings, including an aggressive post-hepatectomy model, as well as tumors driven by hydrodynamic delivery of MYC/CTNNB1-Δ90 oncogenes to the liver, a well-established ICI-refractory HCC model, without signs of hepatic or systemic toxicities in all cases. This effect was accompanied by a significant increase in intratumoral $CD8^+$ T cell infiltration, reinforcing the role of G9a inhibition in enhancing cytotoxic T-cell-mediated tumor clearance. Beyond quantitative changes in lymphocyte infiltration, G9a inhibition profoundly reshaped the TME toward a less immunosuppressive and more immunostimulatory state. Combination therapy promoted the accumulation of both $CD8^+$ and $CD4^+$ T cells while preserving effector memory subsets and avoiding the induction of overt T cell exhaustion, as evidenced by stable LAG-3 expression and only modest increases in PD1. Concomitantly, regulatory T cells and MDSCs were reduced, alleviating key immunosuppressive barriers within the tumor niche. At the myeloid level, G9a inhibition increased dendritic cell frequencies and induced phenotypic reprogramming of TAMs and monocytes toward a more inflammatory, antigen-presenting state, characterized by increased MHC class II and CD86 expression and reduced Arg1 levels.

In summary, our findings implicate G9a as a central regulator of immune escape in HCC and a contributor to resistance to immune checkpoint inhibition. G9a inhibition not only enhances the immunogenicity of HCC cells through transcriptional and epigenetic remodeling but also synergizes with IFN-γ to amplify antigen presentation and chemokine-driven immune cell recruitment. When combined with anti-PD1 therapy, G9a inhibition results in potent antitumor activity and durable immune responses *in vivo*. Together with previous reports demonstrating enhanced $CD8^+$ T cell cytotoxicity upon G9a inhibition, our study supports a compelling rationale for integrating G9a-targeting agents into combination immunotherapy strategies (Graphical Abstract). Given the efficacy, potency, and favorable safety profile of CM272 and EZM8266, these agents represent promising candidates for clinical development as adjuncts to current immunotherapeutic regimens in HCC.

Limitations of the study

Although pharmacologic G9a inhibition reshaped multiple immune populations within the TME, our study does not formally dissect the cell-type-specific contribution of G9a across individual TME compartments. The relative influence of tumor cell intrinsic G9a activity versus its function in $CD8^+$ T cells, DCs, macrophages, or other myeloid subsets remains to be precisely defined. Future studies employing conditional, lineage-restricted genetic models will be essential to resolve these context-dependent roles and refine therapeutic targeting strategies. Despite the use of orthotopic, inflammatory, and MYC/β-catenin-driven models, our systems do not fully recapitulate the chronic liver injury and fibrosis underlying most human HCC cases. Evaluating G9a inhibition in fibrosis or MASH-driven models will be critical to determine its efficacy and safety within a chronically damaged hepatic microenvironment. Finally, our combinatorial approach was restricted to anti-PD1 therapy. Given that current first-line regimens frequently include anti-VEGF-based

combinations or dual immune checkpoint blockade, systematic evaluation of G9a inhibition within these contemporary therapeutic frameworks will be important to define its optimal clinical positioning.

RESOURCE AVAILABILITY

Lead contact

Further information and requests for resources and reagents should be directed to and will be fulfilled by the lead contact, Maite G. Fernandez-Barrena (magarfer@unav.es).

Materials availability

This study did not generate new unique reagents. All materials used in this study are available from the lead contact without restriction.

Data and code availability

- The data and material generated and analyzed during this study, whether produced or examined, are thoroughly included within the main text and accompanying key resources table and STAR Methods. The raw transcriptomics data have been deposited at GEO (accession number GEO: GSE319486) and are publicly available as of the date of publication. The raw data and publicly available datasets used in this study are listed in the key resources table.
- This paper does not report original code.
- Any additional information required to reanalyze the data reported in this work paper is available from the lead contact upon request.

ACKNOWLEDGMENTS

This work was supported by grants from the Scientific Foundation, Spanish Association Against Cancer (AECC): LABAE20011GARC (M.G.F.-B.), PRYCO223102ARM (M.G.F.-B., M.A., C.B., and M.A.A.), PRYGN223117LLOV (J.M.L.), AECC-IDIBAPS Excellence Program Ref. EPAEC246711CLIN (J.M.L.), and ASPIRE-AECC RETOS245779LLOV (J.M.L., M.G.F.-B., M.A., C.B., and M.A.A.); grants from Ministerio de Ciencia Innovación y Universidades MICINN-Agencia Estatal de Investigación integrado en el Plan Estatal de Investigación Científica y Técnica y Innovación, cofinanciado con Fondos FEDER PID2022-139365OB-I00 (R.P.), PID2022-139365OB-I00 (J.M.L.), PID2022-136616OB-I00/AEI/10.13039/501100011033 (M.A.A.), and PID2020-117116RB-I00 (M.G.F.-B.); grant from Instituto de Salud Carlos III (ISCIII) and co-funded by the European Union, PI23/00190 and by Gobierno de Navarra Project Grant 22-2024 (P.S.); grant "Immune4all" PMP2200054 (C.B., M.G.F.-B., M.A., M.A.A.), Generalitat de Catalunya (AGAUR, 2021-SGR 01347), and 'la Caixa' Foundation under the agreement LCF/PR/SP23/52950009 (J.M.L.); grants from the European Commission (Horizon Europe-Mission Cancer, THRIVE, Ref. 101136622), an Accelerator Award from Cancer Research UK, Fondazione per la Ricerca sul Cancro (AIRC), Fundación Científica de la Asociación Española Contra el Cáncer (FAECC) (HUNTER, Ref. C9380/A26813), the NIH (R01-CA273932–01, R01DK56621, and R01DK128289), the Samuel Waxman Cancer Research Foundation (J.M.L.), Predoctoral Juan Serra fellowship (BCU), Ministerio de Ciencia, Innovación y Universidades, Programa de Formación del Profesorado Universitario, FPU predoctoral fellowship (G.C.-S. and E.A.-V.), predoctoral fellowship PREP2022-000609 (PID2022-136616OB-I00) financiada por MICIU/AEI/10.13039/501100011033 y por el FSE (E.V.-G.), the Saastamoinen Foundation (A.H.S.), and the Marie Skłodowska-Curie Actions of the European Comission; grant agreement HORIZON-MSCA-2024-PF-101211997 (A.H.S.). AECC investigador fellowship INVES223049AREC (M.A.), Sara Borrell Contract CD22/00109 from Spanish Ministry of Health (A.L.-P.), and Ramón y Cajal Program contract RYC2018-024475-1 funded by MCIU/AEI/10.13039/501100011033 and ESF "Investing in your future" (M.G.F.-B.). Epizyme (an Ipsen company) provided the compound, EZM8266. A.C. is an employee of Ipsen at the time of submission, and V.G. was an employee of Epizyme (an Ipsen company) at the time of writing the manuscript.

We thank Ms. Laura Alvarez for her expert technical assistance. We thank Mr. Eduardo Ávila for his generous support. This study has been developed in part in the Center Esther Koplowitz from IDIBAPS/CERCA Program/Generalitat de Catalunya. The work was also supported in part through the computational and data resources and staff expertise provided by Scientific Computing and Data at the Icahn School of Medicine at Mount Sinai and supported by the Clinical and Translational Science Awards (CTSA) grant UL1TR004419 from the National Center for Advancing Translational Sciences. Research reported in this publication was also supported by the Office of Research Infrastructure of the National Institutes of Health under award numbers S10OD026880 and S10OD030463. The content is solely the responsibility of the authors and does not necessarily represent the official views of the National Institutes of Health.

AUTHOR CONTRIBUTIONS

Conception and design, U.V.-G., F.P., B.S., J.A., R.P., J.M.L., M.A., C.B., M.A.A., and M.G.F.-B. Development of methodology, E.A.-V., B.C.-U., I.U., E.S., R.B., M.B., A.L.-P., M.U.L., J.E., E.V.-G., A.M., A.G.-O., G.C.-S., L.N., and S.C. Acquisition of data, E.A.-V., B.C.-U., I.U., R.B., M.B., J.E., P.B., P.S., A.M., A.H.d.S., L.N., S.C., and R.P. Analysis and interpretation of data (statistical analysis, biostatistics, and computational analysis), B.C.-U., E.A.-V., I.U., A.L.-P., P.B., P.S., J.M.L., C.B., M.A., M.A.A., and M.G.F.-B. Writing—review and/or revision of manuscript, E.A.-V., B.S., I.U., M.A.A., and M.G.F.-B. Administrative, technical, or material support, A.C., V.G., B.S., E.S., J.A., R.P., and J.M.L. All authors read and approved the final manuscript.

DECLARATION OF INTERESTS

J.M.L. reports research support from Genentech and Roche; consultancy/sponsored lectures from Eisai Inc., Merck, Roche, Genentech, AstraZeneca, Bayer Pharmaceuticals, Abbvie, Sanofi, Moderna, Glycotest, Exelixis, and Boehringer Ingelheim; and Data Safety Monitoring Board for Industry or Commercial Enterprise from Bristol Myers Squibb.

STAR★METHODS

Detailed methods are provided in the online version of this paper and include the following:

- KEY RESOURCES TABLE
- EXPERIMENTAL MODEL AND STUDY PARTICIPANT DETAILS
  - HCC cell lines
  - Preclinical mouse models
- METHOD DETAILS
  - Transcriptomic data acquisition and preprocessing
  - Molecular classification and gene expression analysis
  - Cell culture, treatments and reagents
  - RNA isolation, quantitative real-time PCR (RT-qPCR) and RNA sequencing (RNAseq)
  - RNAseq analysis
  - Identification and differential analysis of transposable elements (TE)
  - Colony formation, anchorage-independent growth, migration and invasion assays
  - Enzyme-linked immunosorbent assay (ELISA)
  - Flow cytometry
  - Immunofluorescence
  - Chromatin immunoprecipitation (ChIP)
  - *In vivo* experiments
  - Biochemical parameters
  - Immunohistochemical analyses
- QUANTIFICATION AND STATISTICAL ANALYSIS

SUPPLEMENTAL INFORMATION

Supplemental information can be found online at https://doi.org/10.1016/j.xcrm.2026.102717.

Received: July 27, 2025
Revised: February 3, 2026
Accepted: March 3, 2026

REFERENCES

1. Rumgay, H., Arnold, M., Ferlay, J., Lesi, O., Cabasag, C.J., Vignat, J., Laversanne, M., McGlynn, K.A., and Soerjomataram, I. (2022). Global burden of primary liver cancer in 2020 and predictions to 2040. J. Hepatol. *77*, 1598–1606. https://doi.org/10.1016/J.JHEP.2022.08.021.
2. Singal, A.G., Kanwal, F., and Llovet, J.M. (2023). Global trends in hepatocellular carcinoma epidemiology: implications for screening, prevention and therapy. Nat. Rev. Clin. Oncol. *20*, 864–884. https://doi.org/10.1038/S41571-023-00825-3.
3. Llovet, J.M., Castet, F., Heikenwalder, M., Maini, M.K., Mazzaferro, V., Pinato, D.J., Pikarsky, E., Zhu, A.X., and Finn, R.S. (2022). Immunotherapies for hepatocellular carcinoma. Nat. Rev. Clin. Oncol. *19*, 151–172. https://doi.org/10.1038/S41571-021-00573-2.
4. Llovet, J.M., Pinyol, R., Yarchoan, M., Singal, A.G., Marron, T.U., Schwartz, M., Pikarsky, E., Kudo, M., and Finn, R.S. (2024). Adjuvant and neoadjuvant immunotherapies in hepatocellular carcinoma. Nat. Rev. Clin. Oncol. *21*, 294–311. https://doi.org/10.1038/S41571-024-00868-0.
5. Eghbali, S., and Heumann, T.R. (2025). Next-Generation Immunotherapy for Hepatocellular Carcinoma: Mechanisms of Resistance and Novel Treatment Approaches. Cancers (Basel) *17*, 236. https://doi.org/10.3390/CANCERS17020236.
6. Manfredi, G.F., Celsa, C., John, C., Jones, C., Acuti, N., Scheiner, B., Fulgenzi, C.A.M., Korolewicz, J., Pinter, M., Gennari, A., et al. (2023). Mechanisms of Resistance to Immunotherapy in Hepatocellular Carcinoma. J. Hepatocell. Carcinoma *10*, 1955–1971. https://doi.org/10.2147/JHC.S291553.
7. Alsaafeen, B.H., Ali, B.R., and Elkord, E. (2025). Resistance mechanisms to immune checkpoint inhibitors: updated insights. Mol. Cancer *24*, 20. https://doi.org/10.1186/S12943-024-02212-7.
8. Liu, Y., Yang, H., Li, T., and Zhang, N. (2024). Immunotherapy in liver cancer: overcoming the tolerogenic liver microenvironment. Front. Immunol. *15*, 1460282. https://doi.org/10.3389/FIMMU.2024.1460282/PDF.
9. Fernández-Barrena, M.G., Arechederra, M., Colyn, L., Berasain, C., and Avila, M.A. (2020). Epigenetics in hepatocellular carcinoma development and therapy: The tip of the iceberg. JHEP Rep. *2*, 100167. https://doi.org/10.1016/j.jhepr.2020.100167.
10. Braghini, M.R., Lo Re, O., Romito, I., Fernandez-Barrena, M.G., Barbaro, B., Pomella, S., Rota, R., Vinciguerra, M., Avila, M.A., and Alisi, A. (2022). Epigenetic remodelling in human hepatocellular carcinoma. J. Exp. Clin. Cancer Res. *41*, 107. https://doi.org/10.1186/S13046-022-02297-2.
11. Bueloni, B., Garcia Fernandez De Barrena, M., Avila, M.A., Bayo, J., and Mazzolini, G. (2025). Epigenetic mechanisms involved in hepatocellular carcinoma development and progression. eGastroenterology *3*, e100186. https://doi.org/10.1136/EGASTRO-2025-100186.
12. Castelló-Uribe, B., López-Pascual, A., Elurbide, J., Adán-Villaescusa, E., Valbuena-Goiricelaya, E., Martinez-Perez, L.A., Uriarte, I., Latasa, M.U., Sangro, B., Arechederra, M., et al. (2025). Expression landscape of epigenetic genes in human hepatocellular carcinoma. J. Physiol. Biochem. *81*, 699–727. https://doi.org/10.1007/S13105-025-01095-6.
13. Donne, R., and Lujambio, A. (2023). The liver cancer immune microenvironment: Therapeutic implications for hepatocellular carcinoma. Hepatology *77*, 1773–1796. https://doi.org/10.1002/HEP.32740.
14. Hong, Y.K., Li, Y., Pandit, H., Li, S., Pulliam, Z., Zheng, Q., Yu, Y., and Martin, R.C.G. (2019). Epigenetic modulation enhances immunotherapy for hepatocellular carcinoma. Cell. Immunol. *336*, 66–74. https://doi.org/10.1016/j.cellimm.2018.12.010.
15. Tao, S., Liang, S., Zeng, T., and Yin, D. (2022). Epigenetic modification-related mechanisms of hepatocellular carcinoma resistance to immune checkpoint inhibition. Front. Immunol. *13*, 1043667. https://doi.org/10.3389/FIMMU.2022.1043667/XML/NLM.
16. Bárcena-Varela, M., Caruso, S., Llerena, S., Álvarez-Sola, G., Uriarte, I., Latasa, M.U., Urtasun, R., Rebouissou, S., Alvarez, L., Jimenez, M., et al. (2019). Dual Targeting of Histone Methyltransferase G9a and DNA-Methyltransferase 1 for the Treatment of Experimental Hepatocellular Carcinoma. Hepatology *69*, 587–603. https://doi.org/10.1002/hep.30168.
17. Fu, J., Yu, M., Xu, W., and Yu, S. (2023). High Expression of G9a Induces Cisplatin Resistance in Hepatocellular Carcinoma. Cell J. *25*, 118–125. https://doi.org/10.22074/CELLJ.2022.557564.1077.
18. Barcena-Varela, M., Paish, H., Alvarez, L., Uriarte, I., Latasa, M.U., Santamaria, E., Recalde, M., Garate, M., Claveria, A., Colyn, L., et al. (2021). Epigenetic mechanisms and metabolic reprogramming in fibrogenesis: Dual targeting of G9a and DNMT1 for the inhibition of liver fibrosis. Gut *70*, 388–400. https://doi.org/10.1136/gutjnl-2019-320205.
19. Clavería-Cabello, A., Herranz, J.M., Latasa, M.U., Arechederra, M., Uriarte, I., Pineda-Lucena, A., Prosper, F., Berraondo, P., Alonso, C., Sangro, B., et al. (2023). Identification and experimental validation of druggable epigenetic targets in hepatoblastoma. J. Hepatol. *79*, 989–1005. https://doi.org/10.1016/j.jhep.2023.05.031.
20. Oyon, D., Lopez-Pascual, A., Castello-Uribe, B., Uriarte, I., Orsi, G., Llorente, S., Elurbide, J., Adan-Villaescusa, E., Valbuena-Goiricelaya, E., Irigaray-Miramon, A., et al. (2025). Targeting of the G9a, DNMT1 and UHRF1 epigenetic complex as an effective strategy against pancreatic ductal adenocarcinoma. J. Exp. Clin. Cancer Res. *44*, 13. https://doi.org/10.1186/S13046-024-03268-5.
21. Nguyen, L.L., Watson, Z.L., Ortega, R., Woodruff, E.R., Jordan, K.R., Iwanaga, R., Yamamoto, T.M., Bailey, C.A., To, F., Jeong, A.D., et al. (2024). Combining EHMT and PARP Inhibition: A Strategy to Diminish Therapy-Resistant Ovarian Cancer Tumor Growth while Stimulating Immune Activation. Mol. Cancer Ther. *23*, 1332–1347. https://doi.org/10.1158/1535-7163.MCT-23-0613.
22. Montironi, C., Castet, F., Haber, P.K., Pinyol, R., Torres-Martin, M., Torrens, L., Mesropian, A., Wang, H., Puigvehi, M., Maeda, M., et al. (2023). Inflamed and non-inflamed classes of HCC: A revised immunogenomic classification. Gut *72*, 129–140. https://doi.org/10.1136/GUTJNL-2021-325918.
23. Haber, P.K., Castet, F., Torres-Martin, M., Andreu-Oller, C., Puigvehí, M., Miho, M., Radu, P., Dufour, J.F., Verslype, C., Zimpel, C., et al. (2023). Molecular Markers of Response to Anti-PD1 Therapy in Advanced Hepatocellular Carcinoma. Gastroenterology *164*, 72–88.e18. https://doi.org/10.1053/j.gastro.2022.09.005.
24. Ayers, M., Lunceford, J., Nebozhyn, M., Murphy, E., Loboda, A., Kaufman, D.R., Albright, A., Cheng, J.D., Kang, S.P., Shankaran, V., et al. (2017). IFN-γ-related mRNA profile predicts clinical response to PD-1 blockade. J. Clin. Investig. *127*, 2930–2940. https://doi.org/10.1172/JCI91190.
25. Zeng, Q., Klein, C., Caruso, S., Loménie, N., Allende, D.S., Mínguez, B., Iavarone, M., Ningarhari, M., Casadei-Gardini, A., Pedica, F., et al. (2023). Artificial intelligence-based pathology as a biomarker of sensitivity to atezolizumab–bevacizumab in patients with hepatocellular carcinoma: a multicentre retrospective study. Lancet Oncol. *24*, 1411–1422. https://doi.org/10.1016/S1470-2045(23)00468-0.
26. Cappuyns, S., Philips, G., Vandecaveye, V., Boeckx, B., Schepers, R., Van Brussel, T., Arijs, I., Mechels, A., Bassez, A., Lodi, F., et al. (2023). PD-1-CD45RA+ effector-memory CD8 T cells and CXCL10+ macrophages are associated with response to atezolizumab plus bevacizumab in advanced hepatocellular carcinoma. Nat. Commun. *14*, 7825. https://doi.org/10.1038/S41467-023-43381-1.

27. Cappuyns, S., Piqué-Gili, M., Esteban-Fabró, R., Philips, G., Balaseviciute, U., Pinyol, R., Gris-Oliver, A., Vandecaveye, V., Abril-Fornaguera, J., Montironi, C., et al. (2024). Single-cell RNA sequencing-derived signatures define response patterns to atezolizumab + bevacizumab in advanced hepatocellular carcinoma. J. Hepatol. *82*. https://doi.org/10.1016/J.JHEP.2024.12.016.

28. Sangro, B., Melero, I., Wadhawan, S., Finn, R.S., Abou-Alfa, G.K., Cheng, A.L., Yau, T., Furuse, J., Park, J.W., Boyd, Z., et al. (2020). Association of inflammatory biomarkers with clinical outcomes in nivolumab-treated patients with advanced hepatocellular carcinoma. J. Hepatol. *73*, 1460–1469. https://doi.org/10.1016/J.JHEP.2020.07.026.

29. Charoentong, P., Finotello, F., Angelova, M., Mayer, C., Efremova, M., Rieder, D., Hackl, H., and Trajanoski, Z. (2017). Pan-cancer Immunogenomic Analyses Reveal Genotype-Immunophenotype Relationships and Predictors of Response to Checkpoint Blockade. Cell Rep. *18*, 248–262. https://doi.org/10.1016/j.celrep.2016.12.019.

30. Davoli, T., Uno, H., Wooten, E.C., and Elledge, S.J. (2017). Tumor aneuploidy correlates with markers of immune evasion and with reduced response to immunotherapy. Science *355*, eaaf8399. https://doi.org/10.1126/SCIENCE.AAF8399.

31. Cabrita, R., Lauss, M., Sanna, A., Donia, M., Skaarup Larsen, M., Mitra, S., Johansson, I., Phung, B., Harbst, K., Vallon-Christersson, J., et al. (2020). Tertiary lymphoid structures improve immunotherapy and survival in melanoma. Nature *577*, 561–565. https://doi.org/10.1038/S41586-019-1914-8.

32. Lachenmayer, A., Alsinet, C., Savic, R., Cabellos, L., Toffanin, S., Hoshida, Y., Villanueva, A., Minguez, B., Newell, P., Tsai, H.W., et al. (2012). Wnt-pathway activation in two molecular classes of hepatocellular carcinoma and experimental modulation by sorafenib. Clin. Cancer Res. *18*, 4997–5007. https://doi.org/10.1158/1078-0432.CCR-11-2322.

33. Ruiz de Galarreta, M., Bresnahan, E., Molina-Sánchez, P., Lindblad, K.E., Maier, B., Sia, D., Puigvehi, M., Miguela, V., Casanova-Acebes, M., Dhainaut, M., et al. (2019). β-Catenin Activation Promotes Immune Escape and Resistance to Anti-PD-1 Therapy in Hepatocellular Carcinoma. Cancer Discov. *9*, 1124–1141. https://doi.org/10.1158/2159-8290.CD-19-0074.

34. Artal-Martinez de Narvajas, A., Gomez, T.S., Zhang, J.-S., Mann, A.O., Taoda, Y., Gorman, J.A., Herreros-Villanueva, M., Gress, T.M., Ellenrieder, V., Bujanda, L., et al. (2013). Epigenetic regulation of autophagy by the methyltransferase G9a. Mol. Cell Biol. *33*, 3983–3993. https://doi.org/10.1128/MCB.00813-13.

35. Shankar, S.R., Bahirvani, A.G., Rao, V.K., Bharathy, N., Ow, J.R., and Taneja, R. (2013). G9a, a multipotent regulator of gene expression. Epigenetics *8*, 16–22. https://doi.org/10.4161/epi.23331.

36. Casciello, F., Windloch, K., Gannon, F., and Lee, J.S. (2015). Functional Role of G9a Histone Methyltransferase in Cancer. Front. Immunol. *6*, 487. https://doi.org/10.3389/fimmu.2015.00487.

37. Kelly, G.M., Al-Ejeh, F., McCuaig, R., Casciello, F., Ahmad Kamal, N., Ferguson, B., Pritchard, A.L., Ali, S., Silva, I.P., Wilmott, J.S., et al. (2021). G9a Inhibition Enhances Checkpoint Inhibitor Blockade Response in Melanoma. Clin. Cancer Res. *27*, 2624–2635. https://doi.org/10.1158/1078-0432.CCR-20-3463.

38. Igarashi, Y., Akiyama, Y., Shimada, S., Watanabe, S., Hatano, M., Kodera, K., Okazaki, K., Tanji, Y., Tsukihara, S., Taniai, T., et al. (2025). Identification and clinical implications of endogenous retrovirus elements suppressed by SETDB1 in hepatocellular carcinoma. JHEP Rep. *7*, 101307. https://doi.org/10.1016/J.JHEPR.2024.101307.

39. Chen, R., Ishak, C.A., and De Carvalho, D.D. (2021). Endogenous retroelements and the viral mimicry response in cancer therapy and cellular homeostasis. Cancer Discov. *11*, 2707–2725. https://doi.org/10.1158/2159-8290.CD-21-0506.

40. Liu, M., Thomas, S.L., DeWitt, A.K., Zhou, W., Madaj, Z.B., Ohtani, H., Baylin, S.B., Liang, G., and Jones, P.A. (2018). Dual inhibition of DNA and histone methyltransferases increases viral mimicry in ovarian cancer cells. Cancer Res. *78*, 5754–5766. https://doi.org/10.1158/0008-5472.CAN-17-3953.

41. Chiappinelli, K.B., Strissel, P.L., Desrichard, A., Li, H., Henke, C., Akman, B., Hein, A., Rote, N.S., Cope, L.M., Snyder, A., et al. (2015). Inhibiting DNA Methylation Causes an Interferon Response in Cancer via dsRNA Including Endogenous Retroviruses. Cell *162*, 974–986. https://doi.org/10.1016/j.cell.2015.07.011.

42. Maksakova, I.A., Thompson, P.J., Goyal, P., Jones, S.J., Singh, P.B., Karimi, M.M., and Lorincz, M.C. (2013). Distinct roles of KAP1, HP1 and G9a/GLP in silencing of the two-cell-specific retrotransposon MERVL in mouse ES cells. Epigenetics Chromatin *6*, 15. https://doi.org/10.1186/1756-8935-6-15.

43. Raghani, N.R., Chorawala, M.R., Mahadik, M., Patel, R.B., Prajapati, B.G., and Parekh, P.S. (2024). Revolutionizing cancer treatment: comprehensive insights into immunotherapeutic strategies. Med. Oncol. *41*, 51. https://doi.org/10.1007/S12032-023-02280-7.

44. Yoon, S.H., Choi, S.W., Nam, S.W., Lee, K.B., and Nam, J.W. (2021). Preoperative immune landscape predisposes adverse outcomes in hepatocellular carcinoma patients with liver transplantation. npj Precis. Oncol. *5*, 27. https://doi.org/10.1038/S41698-021-00167-2.

45. Son, J.A., Ahn, H.R., You, D., Baek, G.O., Yoon, M.G., Yoon, J.H., Cho, H.J., Kim, S.S., Nam, S.W., Eun, J.W., and Cheong, J.Y. (2022). Novel Gene Signatures as Prognostic Biomarkers for Predicting the Recurrence of Hepatocellular Carcinoma. Cancers (Basel) *14*, 865. https://doi.org/10.3390/CANCERS14040865.

46. Roessler, S., Jia, H.L., Budhu, A., Forgues, M., Ye, Q.H., Lee, J.S., Thorgeirsson, S.S., Sun, Z., Tang, Z.Y., Qin, L.X., and Wang, X.W. (2010). A unique metastasis gene signature enables prediction of tumor relapse in early-stage hepatocellular carcinoma patients. Cancer Res. *70*, 10202–10212. https://doi.org/10.1158/0008-5472.CAN-10-2607.

47. Segovia, C., San José-Enériz, E., Munera-Maravilla, E., Martínez-Fernández, M., Garate, L., Miranda, E., Vilas-Zornoza, A., Lodewijk, I., Rubio, C., Segrelles, C., et al. (2019). Inhibition of a G9a/DNMT network triggers immune-mediated bladder cancer regression. Nat. Med. *25*, 1073–1081. https://doi.org/10.1038/S41591-019-0499-Y.

48. Lam, M.S.Y., Reales-Calderon, J.A., Ow, J.R., Aw, J.J.Y., Tan, D., Vijayakumar, R., Ceccarello, E., Tabaglio, T., Lim, Y.T., Chien, W.L., et al. (2023). G9a/GLP inhibition during ex vivo lymphocyte expansion increases in vivo cytotoxicity of engineered T cells against hepatocellular carcinoma. Nat. Commun. *14*, 563. https://doi.org/10.1038/S41467-023-36160-5.

49. Cao, H., Li, L., Yang, D., Zeng, L., Yewei, X., Yu, B., Liao, G., and Chen, J. (2019). Recent progress in histone methyltransferase (G9a) inhibitors as anticancer agents. Eur. J. Med. Chem. *179*, 537–546. https://doi.org/10.1016/J.EJMECH.2019.06.072.

50. Coward, W.R., Brand, O.J., Pasini, A., Jenkins, G., Knox, A.J., and Pang, L. (2018). Interplay between EZH2 and G9a Regulates CXCL10 Gene Repression in Idiopathic Pulmonary Fibrosis. Am. J. Respir. Cell Mol. Biol. *58*, 449–460. https://doi.org/10.1165/rcmb.2017-0286OC.

51. Zhang, M., Wang, G., Ma, Z., Xiong, G., Wang, W., Huang, Z., Wan, Y., Xu, X., Hoyle, R.G., Yi, C., et al. (2022). BET inhibition triggers antitumor immunity by enhancing MHC class I expression in head and neck squamous cell carcinoma. Mol. Ther. *30*, 3394–3413. https://doi.org/10.1016/j.ymthe.2022.07.022.

52. Fukuda, K., and Shinkai, Y. (2020). SETDB1-Mediated Silencing of Retroelements. Viruses *12*, 596. https://doi.org/10.3390/V12060596.

53. Martin, M. (2011). Cutadapt removes adapter sequences from high-throughput sequencing reads. EMBnet J. *17*, 10–12. https://doi.org/10.14806/ej.17.1.200.

54. Dobin, A., Davis, C.A., Schlesinger, F., Drenkow, J., Zaleski, C., Jha, S., Batut, P., Chaisson, M., and Gingeras, T.R. (2013). STAR: ultrafast universal RNA-seq aligner. Bioinformatics *29*, 15–21. https://doi.org/10.1093/bioinformatics/bts635.

55. Morales, J., Pujar, S., Loveland, J.E., Astashyn, A., Bennett, R., Berry, A., Cox, E., Davidson, C., Ermolaeva, O., Farrell, C.M., et al. (2022). A joint NCBI and EMBL-EBI transcript set for clinical genomics and research. Nature *604*, 310–315. https://doi.org/10.1038/S41586-022-04558-8.

56. Mounir, M., Lucchetta, M., Silva, T.C., Olsen, C., Bontempi, G., Chen, X., Noushmehr, H., Colaprico, A., and Papaleo, E. (2019). New functionalities in the TCGAbiolinks package for the study and integration of cancer data from GDC and GTEx. PLoS Comput. Biol. *15*, e1006701. https://doi.org/10.1371/JOURNAL.PCBI.1006701.

57. Sia, D., Jiao, Y., Martinez-Quetglas, I., Kuchuk, O., Villacorta-Martin, C., Castro de Moura, M., Putra, J., Camprecios, G., Bassaganyas, L., Akers, N., et al. (2017). Identification of an Immune-specific Class of Hepatocellular Carcinoma, Based on Molecular Features. Gastroenterology *153*, 812–826. https://doi.org/10.1053/J.GASTRO.2017.06.007.

58. Villanueva, A., Portela, A., Sayols, S., Battiston, C., Hoshida, Y., Méndez-González, J., Imbeaud, S., Letouzé, E., Hernandez-Gea, V., Cornella, H., et al. (2015). DNA methylation-based prognosis and epidrivers in hepatocellular carcinoma. Hepatology *61*, 1945–1956. https://doi.org/10.1002/hep.27732.

59. Mercatelli, D., Lopez-Garcia, G., and Giorgi, F.M. (2020). corto: a lightweight R package for gene network inference and master regulator analysis. Bioinformatics *36*, 3916–3917. https://doi.org/10.1093/BIOINFORMATICS/BTAA223.

60. Hoshida, Y., Villanueva, A., Kobayashi, M., Peix, J., Chiang, D.Y., Camargo, A., Gupta, S., Moore, J., Wrobel, M.J., Lerner, J., et al. (2008). Gene expression in fixed tissues and outcome in hepatocellular carcinoma. N. Engl. J. Med. *359*, 1995–2004. https://doi.org/10.1056/NEJMoa0804525.

61. Reich, M., Liefeld, T., Gould, J., Lerner, J., Tamayo, P., and Mesirov, J.P. (2006). GenePattern 2.0 [2] (Preprint at Nature Publishing Group). https://doi.org/10.1038/ng0506-500.

62. Barbie, D.A., Tamayo, P., Boehm, J.S., Kim, S.Y., Moody, S.E., Dunn, I.F., Schinzel, A.C., Sandy, P., Meylan, E., Scholl, C., et al. (2009). Systematic RNA interference reveals that oncogenic KRAS-driven cancers require TBK1. Nature *462*, 108–112. https://doi.org/10.1038/nature08460.

63. Rooney, M.S., Shukla, S.A., Wu, C.J., Getz, G., and Hacohen, N. (2015). Molecular and genetic properties of tumors associated with local immune cytolytic activity. Cell *160*, 48–61. https://doi.org/10.1016/j.cell.2014.12.033.

64. Yoshihara, K., Shahmoradgoli, M., Martínez, E., Vegesna, R., Kim, H., Torres-Garcia, W., Treviño, V., Shen, H., Laird, P.W., Levine, D.A., et al. (2013). Inferring tumour purity and stromal and immune cell admixture from expression data. Nat. Commun. *4*, 2612. https://doi.org/10.1038/ncomms3612.

65. Satija, R., Farrell, J.A., Gennert, D., Schier, A.F., and Regev, A. (2015). Spatial reconstruction of single-cell gene expression data. Nat. Biotechnol. *33*, 495–502. https://doi.org/10.1038/NBT.3192.

66. Wickham, H. (2016). ggplot2: Elegant Graphics for Data Analysis (New York: Springer-Verlag).

67. San José-Enériz, E., Agirre, X., Rabal, O., Vilas-Zornoza, A., Sanchez-Arias, J.A., Miranda, E., Ugarte, A., Roa, S., Paiva, B., Estella-Hermoso de Mendoza, A., et al. (2017). Discovery of first-in-class reversible dual small molecule inhibitors against G9a and DNMTs in hematological malignancies. Nat. Commun. *8*, 15424. https://doi.org/10.1038/ncomms15424.

68. Recalde, M., Gárate-Rascón, M., Elizalde, M., Azkona, M., Latasa, M.U., Bárcena-Varela, M., Sangro, B., Fernández-Barrena, M.G., Ávila, M.A., Arechederra, M., and Berasain, C. (2021). The splicing regulator SLU7 is required to preserve DNMT1 protein stability and DNA methylation. Nucleic Acids Res. *49*, 8592–8609. https://doi.org/10.1093/NAR/GKAB649.

69. Nevzorova, Y.A., Tolba, R., Trautwein, C., and Liedtke, C. (2015). Partial hepatectomy in mice. Lab. Anim. *49*, 81–88. https://doi.org/10.1177/0023677215572000.

70. Tampaki, M., Papatheodoridis, G.V., and Cholongitas, E. (2021). Intrahepatic recurrence of hepatocellular carcinoma after resection: an update. Clin. J. Gastroenterol. *14*, 699–713. https://doi.org/10.1007/S12328-021-01394-7.

71. Orci, L.A., Lacotte, S., Delaune, V., Slits, F., Oldani, G., Lazarevic, V., Rossetti, C., Rubbia-Brandt, L., Morel, P., and Toso, C. (2018). Effects of the gut–liver axis on ischaemia-mediated hepatocellular carcinoma recurrence in the mouse liver. J. Hepatol. *68*, 978–985. https://doi.org/10.1016/j.jhep.2017.12.025.

72. Uriarte, I., Santamaria, E., López-Pascual, A., Monte, M.J., Argemí, J., Latasa, M.U., Adán-Villaescusa, E., Irigaray, A., Herranz, J.M., Arechederra, M., et al. (2024). New insights into the regulation of bile acids synthesis during the early stages of liver regeneration: A human and experimental study. Biochim. Biophys. Acta Mol. Basis Dis. *1870*, 167166. https://doi.org/10.1016/j.bbadis.2024.167166.

STAR★METHODS

KEY RESOURCES TABLE

REAGENT or RESOURCE	SOURCE	IDENTIFIER
Antibodies		
CD8 alpha (D4W2Z) Rabbit Monoclonal Antibody - IHQ	Cell Signaling	Cat# 98941; RRID:AB_2756376
Anti-CD4 antibody [EPR19514] - IHQ	Abcam	Cat# ab183685; RRID:AB_2686917
Purified anti-mouse CD16/32 Antibody	BioLegend	Cat# 101302; RRID:AB_312801
FITC anti-mouse H-2Kb Antibody (AF6-88.5)	BioLegend	Cat# 116506; RRID:AB_313733
BUV496 Rat Anti-Mouse CD3 (17A2)	BD Horizon™	Cat# 569671; RRID:AB_3668952
APC/Cyanine7 anti-mouse CD45 Antibody	BioLegend	Cat# 103116; RRID:AB_312981
Alexa Fluor® 700 anti-mouse CD4 Antibody	BioLegend	Cat# 100536; RRID:AB_493701
FITC Rat Anti-Mouse CD8a (53-6.7)	BD Pharmingen™	Cat# 553030; RRID:AB_394568
BUV395 Rat Anti-Mouse CD62L (MEL-14)	BD Biosciences	Cat# 569400; RRID:AB_3685037
BUV661 Rat Anti-Mouse CD44 (IM7)	BD Biosciences	Cat# 741471; RRID:AB_2870939
PerCP/Cyanine5.5 anti-mouse CD279 (PD-1) Antibody (29F.1A12)	BioLegend	Cat# 135208; RRID:AB_2159184
Brilliant Violet 650™ anti-mouse LAG-3 Antibody (C9B7W)	BioLegend	Cat# 125227; RRID:AB_2687209
Brilliant Violet 421™ anti-mouse FOXP3 Antibody (MF-14)	BioLegend	Cat# 126419; RRID:AB_2565933
RY610 Rat Anti-Mouse CD274 (PD-L1) (MIH5)	BD Biosciences	Cat# 758309; RRID:AB_3690451
Brilliant Violet 510™ anti-mouse CD11c Antibody (N418)	BioLegend	Cat# 117338; RRID:AB_2562016
Brilliant Ultra Violet™ 661 CD11b Monoclonal Antibody (M1/70)	Invitrogen	Cat# 376-0112-82; RRID:AB_2925440
BUV395 Rat Anti-Mouse I-A, I-E (2G9)	BD Biosciences	Cat# 569244; RRID:AB_3684900
Brilliant Violet 785™ anti-mouse CD86 Antibody (GL-1)	BioLegend	Cat# 105043; RRID:AB_2566722
Brilliant Violet 421™ anti-mouse F4/80 Antibody (BM8)	BioLegend	Cat# 123132; RRID:AB_11203717
PerCP/Cyanine5.5 anti-mouse CD38 Antibody (90)	BioLegend	Cat# 102722; RRID:AB_2563333
PE anti-mouse Arginase 1 Antibody (W21047I)	BioLegend	Cat# 165804; RRID:AB_3068116
Anti-dsRNA [9D5] - IF	Abcam	Cat# Ab00458–23.0; RRID:AB_2920603
Anti-Histone H3 (di methyl K9) antibody [mAbcam 1220] - IHQ	Abcam	Cat# ab1220; RRID:AB_449854
Anti-EHMT2/G9A antibody [EPR18894] - IHQ	Abcam	Cat# ab185050; RRID:AB_2792982
Anti-IP10 (CXCL10) antibody [EPR20764] - IHQ	Abcam	Cat# ab214668; RRID:AB_3694087
Chemicals, peptides, and recombinant proteins		
CM272	Wuxi	San José-Enériz et al., Nat Commun 8, 15424 (2017). https://doi.org/10.1038/ncomms15424
EZM8266	Epizyme, Ipsen	Patent "Compound 5R" https://patentscope.wipo.int/search/en/detail.jsf?docId¼WO2019079540&_cid¼P10-LS1T2D-13876-1

(*Continued on next page*)

Please cite this article in press as: Adan-Villaescusa et al., Histone methyl-transferase G9a inhibition boosts the efficacy of immune checkpoint inhibitors in experimental hepatocellular carcinoma, Cell Reports Medicine (2026), https://doi.org/10.1016/j.xcrm.2026.102717

Continued

REAGENT or RESOURCE	SOURCE	IDENTIFIER
InVivoMAb anti-mouse PD-1 (CD279)	BioXCell	Cat# BE0146; RRID:AB_10949053
Mouse IFNɣ	Miltenyi Biotec	Cat# 130-105-774
Human IFN-gamma	PeproTech®	Cat# AF-300-02
M-MLV	Invitrogen	Cat# 28025-013
iQ™ SYBR® Green Supermix	BIO-RAD	Cat# 170-8882
Collagenase-D	Roche	Cat# 11088866001
DNAse I	Roche	Cat#1128493001
Lipofectamine RNAiMAX reagent	Invitrogen	Cat# 13778150
EnVision+ System- HRP Labeled Polymer Anti-Rabbit	Dako	Cat# K4003
Liquid DAB+	Dako	Cat# K3468
LIVE/DEAD™ Fixable Near IR (876) Viability Kit	Invitrogen	Cat# L34981
Zombi NIR Fixable viability Kit	BioLegend	Cat #54-423-106
BD Cytofix™ Fixation Buffer	BD Biosciences	Cat# 554655
BD Perm/Wash™ Perm/Wash Buffer	BD Biosciences	Cat# 554723
Foxp3/Transcription Factor Staining Buffer Set	eBioscience	Cat# 00-5523-00
VECTASHIELD Antifade Mounting Medium with DAPI	Vector Laboratories	Cat# H-1800-10
Critical commercial assays		
Mouse CXCL9/MIG DuoSet ELISA	RandD	Cat# DY492
Mouse CXCL10/IP-10/CRG-2 DuoSet ELISA	RandD	Cat# DY466
BD OptEIA™ Human IP-10 ELISA Set	BD Biosciences	Cat# 550926
Maxwell RSC simplyRNA extraction kit	Promega	Cat# AS1340
Deposited data		
Microarray data	Gene Expression Omnibus	GEO: GSE14520 (GPL14520)
Microarray data	Gene Expression Omnibus	GEO: GSE89377
Microarray data	Gene Expression Omnibus	GEO: GSE63898
RNA-seq raw sequencing data	Gene Expression Omnibus	GEO: GSE114564
RNA-seq raw sequencing data	Gene Expression Omnibus	GEO: GSE148355
TCGA-LIHC RNA-seq gene-level raw counts (STAR-Counts)	The Cancer Genome Atlas (TCGA)	GDC Data Portal
Processed scRNA-seq read count data and metadata	Original study	https://lambrechtslab.sites.vib.be/en/aHCC
RNA-seq raw sequencing data (mouse NM53.cells and human PLC/PRF/5 cells)	This paper	GEO: GSE319486
Experimental models: Cell lines		
Mouse: PM299L	Dr. Amaia Lujambio Icahn School of Medicine at Mount Sinai	N/A
Mouse: NM53	In house	N/A
Human: HuH7	Japanese Collection of Research Bioresources (JCRB) Cell Bank	N/A
Human: PLC/PRF/5	ATCC	Cat# CRL-8024 ™
Human: SNU449	ATCC	Cat# CRL-2234 ™
Human: Hep3B	ATCC	Cat# HB-8064 ™
Experimental models: Organisms/strains		
Mouse: C57BL/6J	Jackson Laboratory	Cat# 000664

(*Continued on next page*)

Please cite this article in press as: Adan-Villaescusa et al., Histone methyl-transferase G9a inhibition boosts the efficacy of immune checkpoint inhibitors in experimental hepatocellular carcinoma, Cell Reports Medicine (2026), https://doi.org/10.1016/j.xcrm.2026.102717

Continued

REAGENT or RESOURCE	SOURCE	IDENTIFIER
Oligonucleotides		
Primer qRT-PCR: CXCL9 (human) Forward: TGCTGGTTCTGATTGGAGTG; Reverse: TTTGGCTGACCTGTTTCTCC	This paper	N/A
Primer qRT-PCR: Cxcl9 (mouse) Forward: TGGAGTTCGAGGAACCCTAGT; Reverse: TTCCCCCTCTTTTGCTTTTT	This paper	N/A
Primer qRT-PCR: CXCL10 (human) Forward: CCATTCTGATTTGCTGCCTTA; Reverse: TTCTTGATGGCCTTCGATTC	This paper	N/A
Primer qRT-PCR: Cxcl10 (mouse) Forward: AAGTGCTGCCGTCATTTTCT; Reverse: TGCTCATCATTCTTTTTCATCG	This paper	N/A
Primer qRT-PCR: B2M (human) Forward: GTGCTCGCGCTACTCTCTCT; Reverse: AGAAAGACCAGTCCTTGCTGA	This paper	N/A
Primer qRT-PCR: B2m (mouse) Forward: CTGACCGGCCTGTATGCTAT; Reverse: AGAAAGACCAGTCCTTGCTGA	This paper	N/A
Primer qRT-PCR: HLA-A (human) Forward: GTACCGGCAGGACGCCTA; Reverse: GTGATCTCCGCAGGGTAGAA	This paper	N/A
Primer qRT-PCR: HLA-A (H2-Q2 mouse) Forward: GATTACCTCGCCCTGAATGA; Reverse: GGTCTCCACAAGCTCCATGT	This paper	N/A
Primer qRT-PCR: NLRC5 (human) Forward: TGTGGAGCTGTCTTGTGAGG; Reverse: GGAGCTGAGATTCAGGTTGG	This paper	N/A
Primer qRT-PCR: Nlrc5 (mouse) Forward: AAACCCAGAATGGCTGAGTG; Reverse: GCTCTGAAAAGGACGTTTGG	This paper	N/A
Primer qRT-PCR: MDA5 (IFIH1, human, mouse) Forward: AATGATTTCCGAGAGAAGATGA; Reverse: CCTTTGTGCACCATCATTGTT	This paper	N/A
Primer qRT-PCR: STAT1 (human, mouse) Forward: AGGGGCCATCACATTCACA; Reverse: TTCAGACACAGAAATCAACTCAGTC	This paper	N/A
Primer qRT-PCR: RIGI (human) Forward: GAGCATGCACGAATGAAAGA; Reverse: TTTGCCACGTCCAGTCAATA	This paper	N/A
Primer qRT-PCR: Rigi (mouse) Forward: TGCCTCACTCTTCCTCCAGT; Reverse: CACCTGCCATTCTCCCTTTA	This paper	N/A
Primer qRT-PCR: Casp1 (mouse) Forward: ATCCCACAATGGGCTCTGTT; Reverse: TGTCCTGGGAAGAGGTAGAAA	This paper	N/A
Primer qRT-PCR: Lgals3bp (mouse) Forward: CTGTGGCTCCTCTCTGTGTT; Reverse: ATCGTTGGAGCAGACCAC	This paper	N/A
Primer qRT-PCR: Lgals3bp (mouse) Forward: CTGTGGCTCCTCTCTGTGTT; Reverse: ATCGTTGGAGCAGACCAC	This paper	N/A

(*Continued on next page*)

Continued

REAGENT or RESOURCE	SOURCE	IDENTIFIER
Primer qRT-PCR: Tap1 (mouse) Forward: ACCTGGTTCTGGTTCTCTTGAT; Reverse: CAGTCACCCGAGATGTGATG	This paper	N/A
Primer qRT-PCR: Tap1 (mouse) Forward: ACCTGGTTCTGGTTCTCTTGAT; Reverse: CAGTCACCCGAGATGTGATG	This paper	N/A
Primer qRT-PCR: Irgm2 (mouse) Forward: GACTGGGGACTCTGGCAATG; Reverse: TCTTTCTCATCCTCTGCATGG	This paper	N/A
Primer qRT-PCR: MERVL (mouse) Forward: CTTCCATTCACAGCTGCGACTG; Reverse: CTAGAACCACTCCTGGTACCAAC	Maksakova IA et al. Epigenetics Chromatin. 2013 Jun 4;6(1):15	Maksakova et al.[42]
Primer qRT-PCR: G9a (human) Forward: GCAGCACTGCACGTGTGTGGA; Reverse: ACATCAGCCTCAGCATCAGA	This paper	N/A
Primer qRT-PCR: H3F3 (human, mouse) Forward: AAAGCCGCTCGCAAGAGTGCG; Reverse: ACTTGCCTCCTGCAAAGCAC	This paper	N/A
Primer ChIP: CXCL10 prom (human) Forward: GCTGTACTTCAAGGTTGACTGGT; Reverse: AAGTATGTTACCACCACGCCCTC	Coward WR et al. Am J Respir Cell Mol Biol . 2018	Coward et al.[50]
Primer ChIP: HLA-A prom (human) Forward: GGACCCAGTTCTCACTCCCATT; Reverse: GGGTGCGTGCGGACTTTAGAAC	Zhang M et al. Mol Ther. 2022 Nov 2;30(11):3394-3413	Zhang et al.[51]
Primer ChIP: HLA-B prom (human) Forward: GCTTCATCTCAGTGGGCTACGT; Reverse: TGTGTTCCGGTCCCAATACTCC	Zhang M et al. Mol Ther. 2022 Nov 2;30(11):3394-3413	Zhang et al.[51]
Primer ChIP: HLA-C prom (human) Forward: GCGTCGGGTCCTTCTTCCTGAATA; Reverse: GGAGACGCTGATTGGCTTCTCT	Zhang M et al. Mol Ther. 2022 Nov 2;30(11):3394-3413	Zhang et al.[51]
Primer ChIP: HERV-Fc1 LTRa (human) Forward: GCGTCGGGTCCTTCTTCCTGAATA; Reverse: GGAGACGCTGATTGGCTTCTCT	Liu M et al. Cancer Res. 2018 Oct 15;78(20):5754-5766	Liu et al.[40]
Primer ChIP: HERV-Fc1 LTRb (human) Forward: GCGTCGGGTCCTTCTTCCTGAATA; Reverse: GGAGACGCTGATTGGCTTCTCT	Liu M et al. Cancer Res. 2018 Oct 15;78(20):5754-5766	Liu et al.[40]
Primer ChIP: MLT1N2 (human) Forward: AATTGTGTGGGTTGGCAAGT; Reverse: GAATCTCTCTGAAGAAGCAGCA	Liu M et al. Cancer Res. 2018 Oct 15;78(20):5754-5766	Liu et al.[40]
Primer ChIP: IGS rDNA (human) Forward: TCAGACTTTTCTCTCGGTCACG; Reverse: GAAGTCGAGGAGACTTATCGGG	Liu M et al. Cancer Res. 2018 Oct 15;78(20):5754-5766	Liu et al.[40]
Primer ChIP:ACTBp (human) Forward: GAGGGGAGAGGGGGTAAAA; Reverse: TCGAGCCATAAAAGGCAACT	Liu M et al. Cancer Res. 2018 Oct 15;78(20):5754-5766	Liu et al.[40]
Recombinant DNA		
pT3-EFIa-MYC-IRES-luciferase	Dr. Amaia Lujambio Icahn School of Medicien at Mount Sinai	RRID:Addgene_129775

(*Continued on next page*)

Please cite this article in press as: Adan-Villaescusa et al., Histone methyl-transferase G9a inhibition boosts the efficacy of immune checkpoint inhibitors in experimental hepatocellular carcinoma, Cell Reports Medicine (2026), https://doi.org/10.1016/j.xcrm.2026.102717

Continued

REAGENT or RESOURCE	SOURCE	IDENTIFIER
pCMV-SB13	Dr. Amaia Lujambio Icahn School of Medicien at Mount Sinai	N/A
pT3-N90-CTNNB1 (CTNNB1)	Dr. Amaia Lujambio Icahn School of Medicien at Mount Sinai	N/A
Software and algorithms		
Prism 10 Version 10.4.1 (532)	GraphPad	https://www.graphpad.com/scientific-software/prism/
FlowJo (V10)	BD Life Sciences.	https://www.flowjo.com/solutions/flowjo
QuPath (v06.0)	QuPath Project	https://qupath.github.io/
SRA Toolkit (v3.1.1)	NCBI	https://github.com/ncbi/sra-tools
TrimGalore (v0.6.0)	Babraham Bioinformatics	https://www.bioinformatics.babraham.ac.uk/projects/trim_galore/
Cutadapt (v1.18)	Cutadapt project	https://cutadapt.readthedocs.io
STAR (v2.7.9a)	Dobin Lab	https://github.com/alexdobin/STAR
TEtrancripts (v2.1.4)	Hammell Lab	https://github.com/mhammell-laboratory/TEtranscripts
R (v4.4.2)	R Core Team	https://www.r-project.org
edgeR (v4.4.1)	Bioconductor	https://bioconductor.org/packages/edgeR/
TCGAbiolinks (v2.34)	Bioconductor	https://bioconductor.org/packages/TCGAbiolinks/
clusterProfiler (v4.14.4)	Bioconductor	https://bioconductor.org/packages/clusterProfiler/
ComplexHeatmap (v2.22.0)	Bioconductor	https://bioconductor.org/packages/ComplexHeatmap/
AnnotationDbi (v1.68.0)	Biococductor	https://bioconductor.org/packages/AnnotationDbi/
org.Hs.e.g.,.db (v3.20.0)	Bioconductor	https://bioconductor.org/packages/org.Hs.eg.db/
corto (v1.2.4)	CRAN	https://cran.r-project.org/package=corto
msigdbr (v7.5.1)	CRAN	https://cran.r-project.org/package=msigdbr
ggplot2 (v3.5.2)	CRAN	https://cran.r-project.org/package=ggplot2
car (v3.1-3)	CRAN	https://cran.r-project.org/package=car
Nearest Template Prediction (GenePattern module)	GenePattern	https://www.genepattern.org/modules/docs/NearestTemplatePrediction/4/
ssGSEA (GenePattern module)	GenePattern	https://gsea-msigdb.github.io/ssGSEA-gpmodule/v10/index.html
ESTIMATE (v1.0.13)	Yoshihara Lab	https://bioinformatics.mdanderson.org/estimate/
Seurat (v5.3.0)	Satija Lab	https://satijalab.org/seurat
Other		
Human reference genome FASTA (hg38, GRCh38.p14)	NCBI	https://www.ncbi.nlm.nih.gov/assembly/GCF_000001405.40
MANE Select gene annotations (v1.4)	Matched Annotation from NCBI and EMBL-EBI	https://ftp.ncbi.nlm.nih.gov/refseq/MANE/MANE_human/release_1.4/
Mouse reference genome FASTA (GENCODE vM37, GRCm39)	GENCODE	https://www.gencodegenes.org/mouse/release_M37.html
Gene annotation file (GENCODE vM37, GTF, GRCm39)	GENCODE	https://www.gencodegenes.org/mouse/release_M37.html
Transposable element annotation file (GRCm39_GENCODE_rmsk_TE.gtf.gz)	TEtranscripts	https://www.dropbox.com/scl/fo/jdpgn6fl8ngd3th3zebap/ACdZkShDC1au-OcklipI5kM/TEtranscripts/TE_GTF
MSigDB gene sets (v2025.1)	Molecular Signatures Database	https://www.gsea-msigdb.org

Cell Reports Medicine
Article

CellPress
OPEN ACCESS

EXPERIMENTAL MODEL AND STUDY PARTICIPANT DETAILS

HCC cell lines

The murine HCC cell line NM53 was derived from tumors generated in mice by hydrodynamic tail vein injection of a transposon vector expressing MYC (pT3-EF1a-MYC), a vector expressing SB13 transposase (CMV-SB13) and a CRISPR-CAS9 vector expressing a single-guide RNA (sgRNA) targeting p53 (px330-sgp53).[33] PM299L murine HCC cell line, kindly provided by Dr. A. Lujambio (Icahn School of Medicine, Mount Sinai, NY, USA) was also derived from tumors generated in mice by hydrodynamic tail vein injection of pT3-EF1a-MYC, the CMV-SB13 vector and a transposon vector expressing activated β-catenin (CTNNB1-Δ90), which presents a deletion of the 90 first amino acids leading to constitutive activation.[33] NM53, PM299L, and human HuH7, PLC/PRF/5, Hep3B and SNU449 HCC cell lines were cultured as described.[16] Human cell lines were authenticated by STR profiling using the AmpFLSTR Identifiler Plus kit (Thermo Fisher Scientific), amplifying 16 loci including amelogenin. All the cell lines were tested for mycoplasma contamination.

Preclinical mouse models

All animals received humane care according to the 'Guide for the Care and Use of Laboratory Animals' written by the National Academy of Sciences and published by the National Institutes of Health (NIH publication 86-23, revised 1985). Protocols were approved by the Animal Care Committee of the University of Navarra and were performed following their guidelines (ethical committee approval #048/22). Animal experiments followed the Animal Research: Reporting of *In Vivo* Experiments (ARRIVE) guidelines (http://www.nc3rs.org.uk/arrive-guidelines), developed by the National Center for the Replacement, Refinement and Reduction of Animals in Research (NC3Rs) to improve standards and reporting of animal research. For all studies 6- to 8-week-old male C57BL/6J mice purchased from Jackson Laboratories (Bar Harbor, ME, USA) were used.

METHOD DETAILS

Transcriptomic data acquisition and preprocessing

Publicly available gene expression profiles of human HCC tissues were retrieved from their respective repositories. In the case of transcriptomic high-throughput (RNAseq) analysis, data corresponding to GEO: GSE114564[45] and GEO: GSE148355[44] were downloaded from the NCBI sequence data archive (SRA) in fastq format using SRA Toolkit Version 3.1.1. Adapter sequences and low-quality reads were removed using Trimgalore Version 0.6.0. with cutadapt Version 1.18.[53] Reads were subsequently aligned to the hg38 reference genome using the splice-aware aligner STAR (version 2.7.9a).[54] Gene level quantification was performed with STAR's quantMode GeneCounts option to count the number of reads mapped to each gene. To ensure consistent and reliable gene expression data, MANE annotations (version 1.4)[55] were utilized. TCGA-LIHC gene expression data generated by the TCGA research network (https://www.cancer.gov/tcga) was retrieved as STAR-counts aligned to the hg38 genome, using TCGAbiolinks R package (version 2.34) in R software Version 4.4.2 (hereafter called R).[56] Microarray data for GEO: GSE14520_GPL3921,[46] GEO: GSE89377[45] were directly downloaded from the processed matrices available in the NCBI repository, for which the gene symbols for each platform were updated using AnnotationDbi version 1.68.0 and org.Hs.e.g.,.db version 3.20.0 packages. For all RNAseq datasets, including TCGA-LIHC, raw counts were normalized using the trimmed mean of M-values (TMM) using edgeR (version 4.4.1). TMM normalization accounts for library size differences and composition biases, ensuring accurate comparisons between samples. Additional cohorts were used to validate our findings, including the Heptromic cohort, which included a total of 228 surgically resected fresh-frozen samples previously collected for which transcriptomic profiling was available, GEO: GSE63898.[22,57,58]

Publicly available scRNA-seq data from advanced HCC patients[26] was utilized for studying response to treatment at both the patient and single-cell level. The initial dataset comprised 97,947 cells from 44 patients treated with diverse therapeutic regimens including immune checkpoint inhibitors (ICI) or TKI. After filtering for therapeutic strategy and availability of response data, we finally employed 20 atezo+beva-treated patients (12 Responders, 8 Non-Responders; 46,023 cells), and 5 TKI-treated patients (2 Responders, 3 Non-Responders; 15,436 cells) for comparison.

Molecular classification and gene expression analysis

To evaluate transcriptomic differences, first, low expression genes were filtered using the filterByExpr function implemented in edgeR, with the default setting. After that, the voom-limma pipeline for differential expression was used. For the assessment of the enrichment of specific genesets, single sample geneset enrichment analysis algorithm (ssGSEA) from the corto package (version 1.2.4)[59] was used. Stratification of the patients into high and low subgroups for each of the signatures was done by using the median of the ssGSEA score. Gene Set Enrichment Analysis (GSEA) was performed in pre-ranked mode using the clusterProfiler R package, with genes ranked by log2 fold change. Gene sets were sourced from the Hallmark and Gene Ontology (GO) collections of the Molecular Signatures Database (MSigDB) via the msigdbr package. For the analysis of the transcriptomic data in our validation cohort ($n = 228$), positivity for previously reported gene signatures was evaluated using the Nearest Template Prediction[60] module from GenePattern.[61] Significant prediction was defined using an adjusted FDR q-value <0.05. Gene expression analysis was performed by using the original counts for each gene (organized as a matrix of integer values). The single-sample gene set enrichment analysis (ssGSEA) GenePattern module was used to assess enrichment of activated pathways/signatures in each sample.[62] A list of the

Please cite this article in press as: Adan-Villaescusa et al., Histone methyl-transferase G9a inhibition boosts the efficacy of immune checkpoint inhibitors in experimental hepatocellular carcinoma, Cell Reports Medicine (2026), https://doi.org/10.1016/j.xcrm.2026.102717

gene signatures used for this study can be found in Table S1. Cytolytic activity was calculated as the geometric mean of the genes granzyme A (GZMA) and perforin-1 (PRF1), as previously described.[63] Richness of the immune infiltrate in tumor tissue was inferred from expression data through the Immune Score obtained from the ESTIMATE software and by applying the 141 gene signature using the ssGSEA methodology.[64] To assess differential gene expression per patient from the scRNA-seq data, a pseudobulk analysis was conducted for the expression *EHMT2*. The Seurat package[65] was used to subset the single-cell object based on treatment, and pseudobulk gene expression was obtained by calculating the mean of the RNA assay per patient. The ggplot2 package[66] was subsequently used for generation of boxplots and visualization. To assess differential gene expression per cell, the FindMarkers function from the Seurat package was used to compare expression from any cell corresponding to a responder patient vs. any cell of a non-responder patient. Log10 expression of *EHMT2* per cell was represented in violin plots using ggplot2 package.[66]

Cell culture, treatments and reagents

Treatment times and dosages in the different experiments are specified throughout the manuscript, with controls receiving equivalent concentrations of dimethyl sulfoxide (DMSO) (always < 0.1% of the final volume). All cells were routinely tested for mycoplasma.

CM272 was synthesized as described previously.[67] EZM8266 was provided by Epizyme (an Ipsen company). The structure and synthesis of EZM8266 are described in the patent as ''Compound 5R'' (Campbell JE, Duncan KW, Mills JEJ, Munchhof MJ. Amine-substituted heterocyclic compounds as Ehmt2 inhibitors, salts thereof, and methods of synthesis thereof. 2019. Available from: https://patentscope.wipo.int/search/en/detail.jsf?docId¼WO2019079540&_cid¼P10- LS1T2D-13876-1.). Recombinant human and mouse IFNγ were from Peprotech and Miltenyi, respectively. The anti-PD1 (αPD1) (clone RMPI-14) and the isotype control antibodies are from Bio X Cell (Lebanon, NH, USA).

Human-specific siRNAs targeting *G9a* and *RIGI*, along with control siRNA (siC), were sourced from Santa Cruz Biotechnology (Santa Cruz, CA). Transfections were carried out using 75 nM of each siRNA with Lipofectamine RNAiMAX reagent (Invitrogen, Grand Island, NY, USA), following the protocol detailed previously[16] and according to the manufacturer's guidelines.

RNA isolation, quantitative real-time PCR (RT-qPCR) and RNA sequencing (RNAseq)

Total RNA was isolated from the cell lines using the automated Maxwell system (Promega, Madison, WI, USA). Quantitative reverse transcription PCR (qRT-PCR) was carried out as previously described and gene expression levels were normalized to the housekeeping gene H3F3A.[16,20] Primer sequences are available upon request.

RNA concentration and integrity were assessed using the Qubit High Sensitivity RNA Assay Kit (Thermo Fisher Scientific, Waltham, MA, USA) and the 4200 Tapestation system equipped with High Sensitivity RNA ScreenTape (Agilent Technologies, Santa Clara, CA, USA). All RNA samples exhibited high integrity, with RNA Integrity Number (RIN) values exceeding 8. Library construction was carried out using the Illumina Stranded mRNA Prep Ligation Kit, following the manufacturer's instructions (Illumina, San Diego, CA, USA). For each sample, 100 ng of total RNA was used. RNA sequencing was conducted as previously described[19] at the Genomics Unit of the Center for Applied Medical Research (CIMA), University of Navarra, Pamplona, Spain.

RNAseq analysis

RNAseq data from both human and mouse samples were first preprocessed using the standardized workflow described above. For human PLC/PRF/5 cells reads were aligned to the hg38 reference genome using STAR and the MANE annotations. In the case of mouse NM53 cells, reads were aligned to the GRCm39 genome using STAR and the GENCODE vM37 GTF annotation. The resulting raw counts were normalized using the trimmed mean of M-values (TMM) using edgeR (version 4.4.1). Differential expression analysis and all subsequent downstream analyses, including pre-ranked Gene Set Enrichment Analysis (GSEA), were conducted as described above.

Identification and differential analysis of transposable elements (TE)

To quantify Transposable Elements (TE) expression at the family level, RNAseq samples were first trimmed using TrimGalore, then aligned to the mouse genome (GRCm39) with STAR, using the corresponding GENCODE vM37 GTF annotation. The resulting unsorted BAM files were used as input for TEtranscripts, which were run in multimapping mode with both the GENCODE vM37 GTF and a pre-generated TE annotation file (GRCm39 GENCODE rmsk TE GTF) to assign read counts to genes and TEs. The generated count tables were then preprocessed by filtering out low-expression features and normalized using the TMM method. Differential expression analysis was performed using edgeR.

Colony formation, anchorage-independent growth, migration and invasion assays

Colony formation assays were conducted using the specified cell lines following previously established protocols.[16] Briefly, a total of 3,000 cells were plated in six-well plates containing complete medium, and treated with EZM8266 (at indicated doses) the following day. Media were refreshed every two days, and cultures were maintained for approximately 15 days until observable differences emerged between treatment conditions. Cells were then washed with PBS, fixed with 4% formaldehyde (Sigma-Aldrich, St. Louis, MO, USA) in PBS for 10 min, and stained using crystal violet. Representative images were captured. Each assay was carried out in at least two independent biological replicates, each with three technical replicates.

The soft agar assay was performed to evaluate anchorage-independent cell growth. Briefly, a base layer of 0.6% agar in complete culture medium was prepared in six-well plates. Once solidified, 5,000 PLC/PRF/5 cells per well were suspended in 0.3% agar mixed with complete medium and plated on top of the base layer. Plates were incubated at 37°C in a humidified CO_2 incubator for 3 weeks in the presence or absence of EZM8266. At the endpoint, colonies were stained with crystal violet and counted under the microscope (Leica, Wetzlar, Germany). Experiments were conducted in triplicate.

For migration and invasion assays, HuH7 cells (10^5) were seeded into the upper chambers of Transwell inserts (Corning, Glendale, AZ, USA) featuring 8.0 μm pore polycarbonate membranes.[19] In both assays, cells were cultured in medium containing 0.5% FBS, while the lower chambers were filled with medium containing 30% FBS to serve as a chemoattractant. Following cell attachment, EZM8266 was applied at the indicated concentrations for 24 h. Membranes were then washed with PBS, fixed with 4% paraformaldehyde for 24 h, rinsed again with PBS, and stained with 0.5% crystal violet in 2% methanol. Each experiment was performed in triplicate. Between 3 and 5 images per Transwell insert were acquired at 5X magnification using an inverted microscope (Leica, Wetzlar, Germany). QuPath software was used for image analysis and quantification.

Enzyme-linked immunosorbent assay (ELISA)

CXCL9 and CXCL10 concentrations were measured in culture supernatants collected at the end of the incubation periods using commercial ELISA kits for mouse CXCL9 (DY492) and CXCL10 (DY466), both from R&D Systems, and an ELISA kit for human CXCL10 (550926) from BD Biosciences (Franklin Lanes, NJ, USA). Assays were performed according to the manufacturers' instructions.

Flow cytometry

For *in vitro* MHC-I measurement, cells were detached from culture plates by gentle trypsin treatment. Cells were pelleted and washed once with phosphate-buffered saline (PBS). Dead cells were stained with Zombie NIR viability dye from BioLegend (San Diego, CA, USA; 423105). To block Fc receptors, cells were incubated with purified anti-mouse CD16/32 antibody (clone 93, BioLegend, 101302). Surface staining was performed using anti-mouse H-2K^b antibody (clone AF6-88.5, BioLegend, 116505). Finally, cells were fixed with BD Cytofix Fixation Buffer (BD Biosciences).

For *in vivo* analysis, liver tumors were extracted from mice, disrupted and enzymatically digested with collagenase D (400 U/mL; Roche) and DNase I (50 μg/mL; Roche) at 37°C for 20–30 min. Tissue digestion was stopped by adding 25 μL of 0.5 M EDTA (Invitrogen) per sample. Samples were then mechanically dissociated, filtered through 70 μm nylon cell strainers (Falcon), and centrifuged to obtain single-cell suspensions. Erythrocytes were lysed using ACK lysis buffer (Gibco, Life Technologies). Cells were resuspended in staining buffer and dead cells were excluded using LIVE/DEAD Fixable Near IR (876) Viability Kit (Invitrogen), according to the manufacturer's instructions. Surface staining was performed using antibody panels designed to characterize myeloid and lymphoid populations (antibodies listed in key resources table). For intracellular staining of lymphoid markers, cells were fixed and permeabilized using the FOXP3/Transcription Factor Staining Buffer Set (eBioscience) and stained intracellularly for 30 min at 4°C. For the myeloid panel, cells were fixed with BD Cytofix Fixation Buffer following permeabilization with BD Perm/Wash Perm/Wash Buffer (BD Biosciences) and finally stained intracellularly for 30 min at 4°C. Samples were acquired on CytoFLEX (Beckman Coulter) flow cytometers. Data analysis was performed using FlowJo software (version 10.8).

Immunofluorescence

For immunofluorescent detection of dsRNA cells were cultured on coverslips. After overnight incubation, cells were treated with CM272 or EZM8266 at the indicated concentrations. Immunofluorescence was performed as previously reported.[68] Briefly, after 48 h treatment, cells were fixed with ice-cold methanol for 15 min at room temperature (RT) and washed twice with PBS. Cells were permeabilized with 0.2% Triton X-100 for 10 min at RT. After washing, coverslips were blocked with Superblocking buffer (Thermo Fisher Scientific) for 1 h at RT and incubated 1 h at RT with anti-dsRNA antibody 9D5, ab00458–2.3 (Absolute Antibody, Cleveland, UK) diluted in 1% BSA in PBS. After washing with 1% BSA in PBS, cells were incubated with fluorophore-conjugated secondary antibody in 1% BSA in PBS for 1 h at RT, washed and stained with vectashield (Vector laboratories, Burlingame, CA, USA) containing DAPI. Images were obtained using the Zeiss Axio Imager.M1 microscope (Zeiss, Oberkochen, Germany).

Chromatin immunoprecipitation (ChIP)

ChIP assays were performed in HuH7 cells treated with vehicle, CM272, EZM8266 with or without IFNγ stimulation in each case. Following treatment, protein-chromatin complexes were crosslinked with 1% formaldehyde for 10 min at room temperature and quenched with 1.25 mM glycine for 5 min. Cells were washed twice with ice-cold PBS containing protease inhibitors and collected by centrifugation (1200 rpm, 5 min). Cell pellets were lysed in LB1 buffer (50 mM HEPES-KOH pH 7.5, 140 mM NaCl, 1 mM EDTA, 10% glycerol, 0.5% NP-40, 0.25% Triton X-100, protease inhibitors) and incubated for 10 min at 4°C. Nuclei were isolated by Dounce homogenization and recovered by centrifugation (3000 g, 10 min, 4°C). Nuclear pellets were washed in LB2 buffer (10 mM Tris-HCl pH 8.0, 200 mM NaCl, 1 mM EDTA, 0.5 mM EGTA, protease inhibitors) and centrifuged under the same conditions. Nuclei were resuspended in LB3 buffer (10 mM Tris-HCl pH 8.0, 100 mM NaCl, 1 mM EDTA, 0.5 mM EGTA, 0.1% sodium deoxycholate, 0.5% N-lauroyl sarcosine, protease inhibitors). Chromatin was sheared by sonication to generate fragments ranging from 200 to 1000 bp. Insoluble material was removed by centrifugation (14,000 rpm, 10 min, 4°C), and chromatin extracts were precleared with pre-equilibrated protein G magnetic beads for 2 h at 4°C. Equivalent amounts of chromatin

were incubated overnight at 4°C with 5 μg of anti-H3K9me2 antibody (ab1220, Abcam) or normal rabbit IgG (2729S, Cell Signaling Technology) as a negative control. Immune complexes were captured by incubation with protein G magnetic beads for 4 h at 4°C with rotation. Beads were sequentially washed at 4°C for 5 min each with low-salt buffer (0.1% SDS, 1% Triton X-100, 2 mM EDTA, 20 mM Tris-HCl pH 8.0, 150 mM NaCl, 0.1 M DTT, protease inhibitors), high-salt buffer (same composition containing 500 mM NaCl), LiCl wash buffer (0.25 M LiCl, 1% NP-40, 1% sodium deoxycholate, 1 mM EDTA, 10 mM Tris-HCl pH 8.0, 0.1 M DTT, protease inhibitors), and twice with TE buffer pH 8.0 (100 mM Tris-HCl pH 8.0, 10 mM EDTA). Chromatin was eluted in 250 μL elution buffer (25 mM Tris-HCl pH 7.5, 5 mM EDTA, 0.5% SDS) for 15 min at room temperature with rotation. Samples were supplemented with 5 M NaCl, Tris-HCl pH 7.0, 0.5 M EDTA pH 8.0, and proteinase K, followed by incubation at 45°C for 1 h and crosslink reversal at 65°C for 4 h. RNA was removed by RNase A treatment for 30 min at 37°C. DNA was purified using the PCR Purification Kit (Qiagen) according to the manufacturer's instructions. Enriched DNA was analyzed by quantitative PCR using the primer sets listed in the key resources table.

In vivo experiments

For the orthotopic tumor model, subcutaneous tumors were first generated with PM299L cells in C57BL/6J mice as described previously.[16] When tumors reached approximately 1 cm in diameter, animals were sacrificed and tumor tissues were sliced into equal fragments of ~1 mm^3. These fragments were orthotopically implanted into the left liver lobes of two groups of C57BL/6J mice via laparotomy. Tumor engraftment was monitored by ultrasound scan (US) using the Vevo 770 High-Resolution Imaging System (VisualSonics, Toronto, Canada), enabling *in vivo* visualization, assessment, and measurement of tumors. When lesions reached ~2 mm^3, mice (n = 5 per group) were randomized into control and treatment groups. Mice received 300 mg/kg (oral gavage) of EZM8266 or the same volume of vehicle (0.1% Tween80 and 0.5% methylcellulose, both from Sigma-Aldrich, in sterile water) for the indicated period of time. Mice were then sacrificed and tumors extracted. In a second orthotopic HCC model, 25,000 PM299L cells were intrahepatically injected in the left liver lobe of C57BL/6J mice. At the indicated times, mice were randomly divided into 4 groups and treated with vehicle (0.5% Methylcellulose+0.1% Tween-80 and human igG isotype, Bio X Cell), EZM8266 (300 mg/kg), anti-PD1 (RMP1-14, Bio X Cell, 100 μg per mouse), or EZM8266 plus anti-PD1 for 4 weeks. EZM8266 was administrated via oral gavage 5 days per week. Anti-PD1 was administrated via intraperitoneal injection once a week. Then, mice were sacrificed and liver tumors extracted. Finally, we implemented a third orthotopic syngeneic experimental model in which the growth of implanted HCC cells is stimulated by a concomitant partial hepatectomy (PH). This model mimics the frequent early tumor recurrence observed in patients undergoing HCC resection.[69–71] To this end, 50,000 PM299L cells in 0.2 mL of PBS were directly injected into the inferior right hepatic lobe remnant after a 33% PH performed essentially as previously described.[72] At the indicated times, mice were randomly divided into 4 groups and treated with vehicle, CM272 (5 mg/kg), anti-PD1 (RMP1-14, Bio X Cell, 100 μg per mouse), or CM272 plus anti-PD1 for 4 weeks. CM272 was administrated via intraperitoneal injection 5 days per week. Anti-PD1 was administrated via intraperitoneal injection once a week. At the indicated time point mice were sacrificed and liver tumors extracted. For the hydrodynamic tail-vein injection model, a sterile 0.9% NaCl solution/plasmid mix was prepared containing DNA. We used 10 μg of pT3-EF1a-MYC (MYC), 10 μg of pT3-N90-CTNNB1 (CTNNB1-ΔN90) and 0.8 μg of SB13 transposase-encoding plasmids dissolved in 2 mL of 0.9% NaCl solution, sterile filtered, and a volume corresponding to 10% of the weight of each mouse in volume was injected into the lateral tail vein of 4 weeks old male C57BL/6J mice as described.[33] At the indicated times, mice were again randomly divided into 6 groups and treated with vehicle, CM272 (5 mg/kg), EZM8266 (300 mg/kg), anti-PD1 (RMP1-14, Bio X Cell, 100 μg per mouse), or CM272 plus anti-PD1 and EZM8266 plus anti-PD1 for 4 weeks. CM272 was administrated via intraperitoneal injection 5 days per week and EZM8266 via oral gavage also 5 days per week. Anti-PD1 was administrated via intraperitoneal injection once a week. At the indicated time point mice were sacrificed and liver tumors extracted.

Biochemical parameters

Serum levels of alanine aminotransferase (ALT), aspartate aminotransferase (AST), and lactate dehydrogenase (LDH) were measured using a C311 Cobas Analyzer (Roche Diagnostics GmbH, Mannheim, Germany) following the manufacturer's instructions.

Immunohistochemical analyses

Immunohistochemical analyses on liver and HCC tissues were performed essentially as described.[16,18,19] Antibodies used were: 98941T from Cell Signaling (Danvers, MA, USA) for CD8, and ab183685 from Abcam (Cambridge, UK) for CD4, both at 1:100 dilution. HRP conjugated Envision secondary antibody (K4003), followed by DAB reagent (K3468), both from DAKO (Glostrup, Denmark), were applied for detection. For signal quantification, images were analyzed with the QuPath software v0.3.217. Tissue sections were counterstained with Hematoxylin (Sigma-Aldrich) and dehydrated. Negative controls were performed omitting primary antibodies.

QUANTIFICATION AND STATISTICAL ANALYSIS

Genes were considered differentially expressed if the adjusted *p*-value, calculated using the Benjamini-Hochberg FDR method, was below 0.05. For correlation analysis of gene expression data Spearman's correlation was used. Statistical analyses were performed using GraphPad Prism software (v10; GraphPad Software Inc., La Jolla, CA, USA). For comparison between two groups, paired two-tailed Student's *t* test, or Kruskal-Wallis ANOVA-test were used according to sample distribution. All reported *p* values were two-tailed and differences were considered significant when $p < 0.05$.

Cell Reports Medicine, Volume *7*

Supplemental information

Histone methyl-transferase G9a inhibition boosts the efficacy of immune checkpoint inhibitors in experimental hepatocellular carcinoma

Elena Adan-Villaescusa, Borja Castello-Uribe, Iker Uriarte, Eva Santamaria, Roberto Barbero, Miriam Belzunce, Amaya López-Pascual, Maria Ujue Latasa, Jasmin Elurbide, Emiliana Valbuena-Goiricelaya, Agavni Mesropian, Guillem Cano-Segarra, Ana Hernández de Sande, Lorenzo Nevi, Simone Carotti, Umberto Vespasiani-Gentilucci, Felipe Prosper, Antonio Pineda-Lucena, Bruno Sangro, Josepmaria Argemi, Pedro Berraondo, Pablo Sarobe, Albert Gris-Oliver, Roser Pinyol, Josep M. Llovet, Maria Arechederra, Carmen Berasain, Alexis Cocozaki, Veronica Gibaja, Matias A. Avila, and Maite G. Fernandez-Barrena

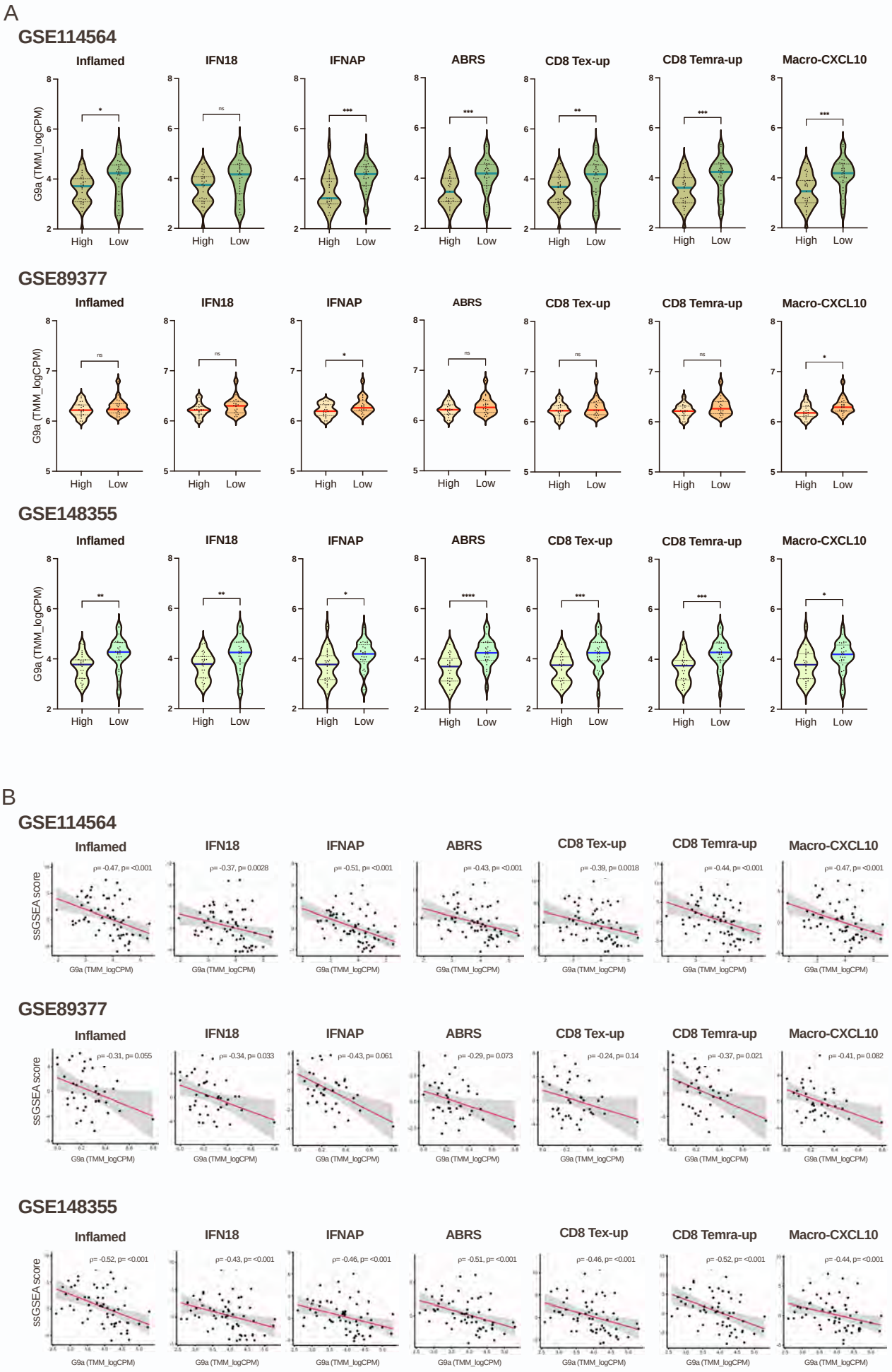

Figure S1. ***G9a expression in HCC tissues is associated with gene signatures predictive of immune-based therapy response.*** (A) *G9a* expression in patients from the GSE89377, GSE114564, GSE148355 HCC gene expression datasets stratified according to the score of the indicated predictive signatures. (B) Spearman correlation plots showing the inverse association between *G9a* gene expression and the indicated signatures, as quantified by ssGSEA scores. Correlation coefficients (Spearman's ρ) and corresponding p-values are indicated in each plot. Related to Figure 1. ** *p<0.01*, *** *p<0.001*, **** *p<0.0001*.

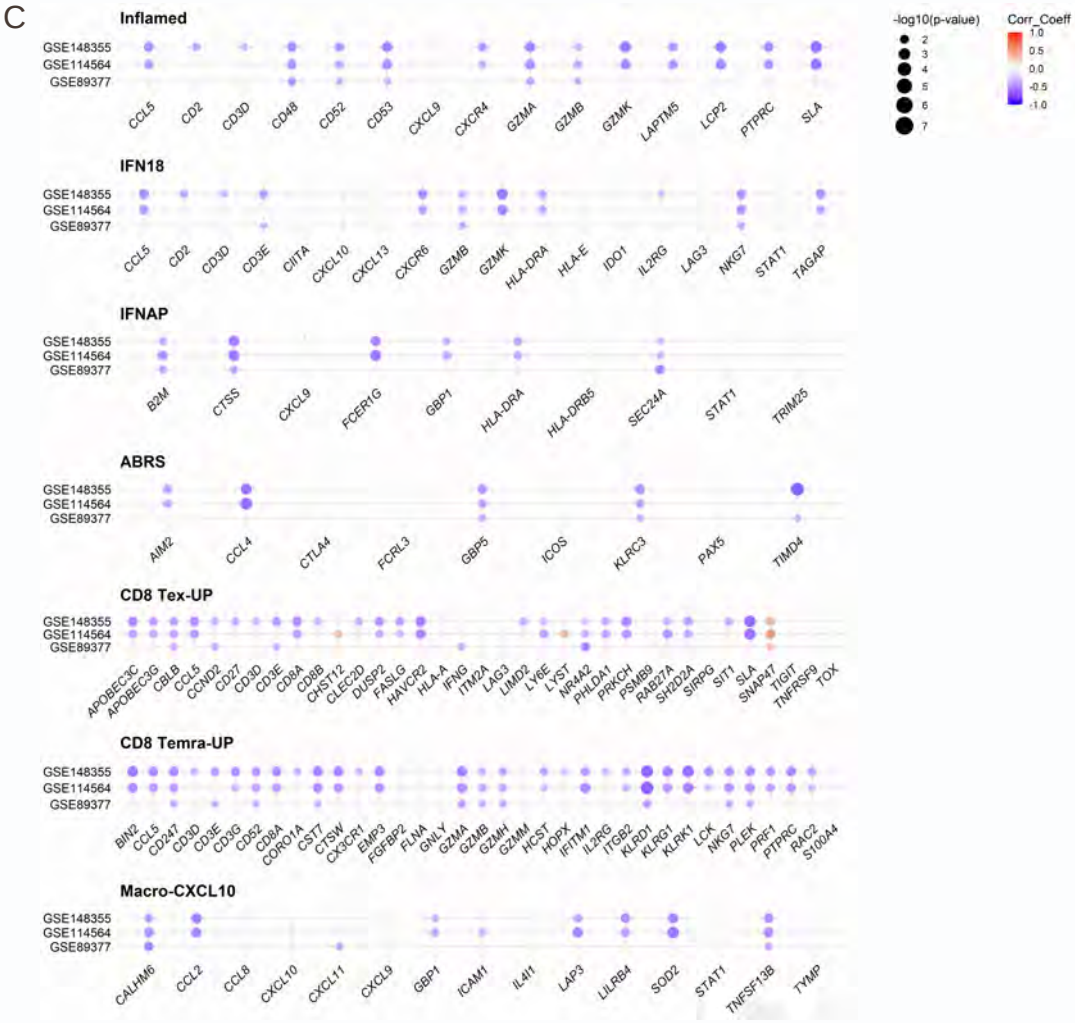

Figure S1. ***G9a expression in HCC tissues is associated with gene signatures predictive of immune-based therapy response.*** (C) Correlation between *G9a* expression and that of the different genes that constitute the indicated predictive signatures in the specified gene expression datasets.Related to Figure 1. ** *p<0.01*, *** *p<0.001*, **** *p<0.0001*.

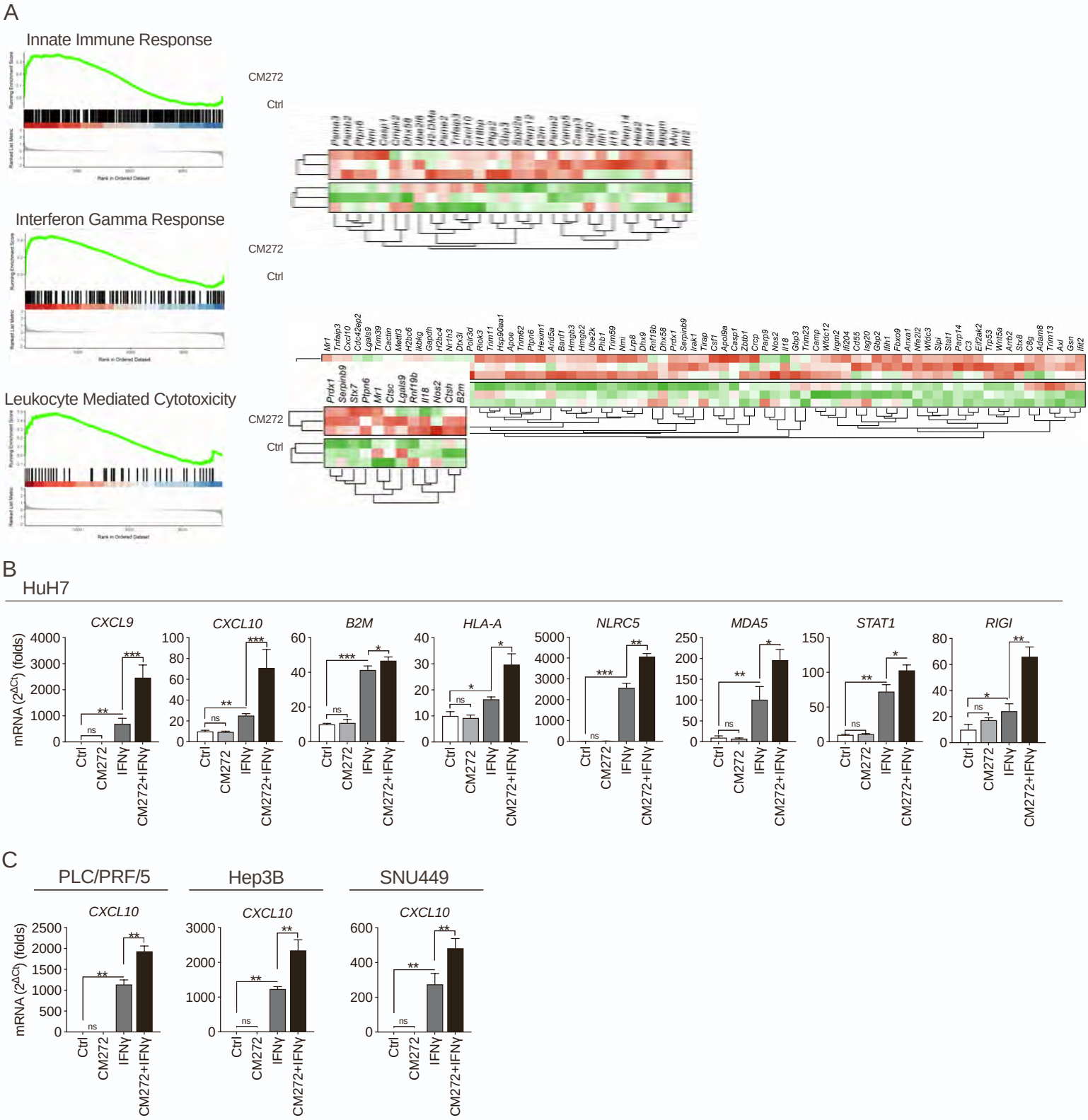

Figure S2. ***G9a inhibition with CM272 enhances the immunogenicity of HCC cells.*** (A) GSEA analysis was performed to compare gene expression profiles between control (Ctrl) and CM272-treated (400 nM for 48 h) NM53 cells. Enrichment plots show increased expression of genes associated with Interferon Gamma Response, Innate Immune Response, and Leukocyte Mediated Cytotoxicity signatures in CM272-NM53 treated cells. Corresponding heatmaps show genes within each signature that are differentially expressed upon CM272 treatment. (B) Validation in human HCC cells (HuH7) of the effects of CM272, INFg and their combination, on the expression of selected genes identified in the RNAseq analyses in the murine HCC cell line PM299L. HuH7 cells were treated with CM272 (400 nM) for 24 h, followed by 24 h of IFNγ stimulation (75 U/mL) as indicated (n=3). (C) *CXCL10* mRNA expression levels of human HCC cell lines PLC/PRF/5, Hep3B and SNU449 cells treated with CM272 (400 nM) for 24 h, followed by 24 h of IFNγ stimulation (75 U/mL) as indicated (n=3). Related to Figure 3. Data are represented as mean +/- SEM. * *p<0.05*, ** *p<0.01*, *** *p<0.001*, **** *p<0.0001*. All the replicates represent biological replicates.

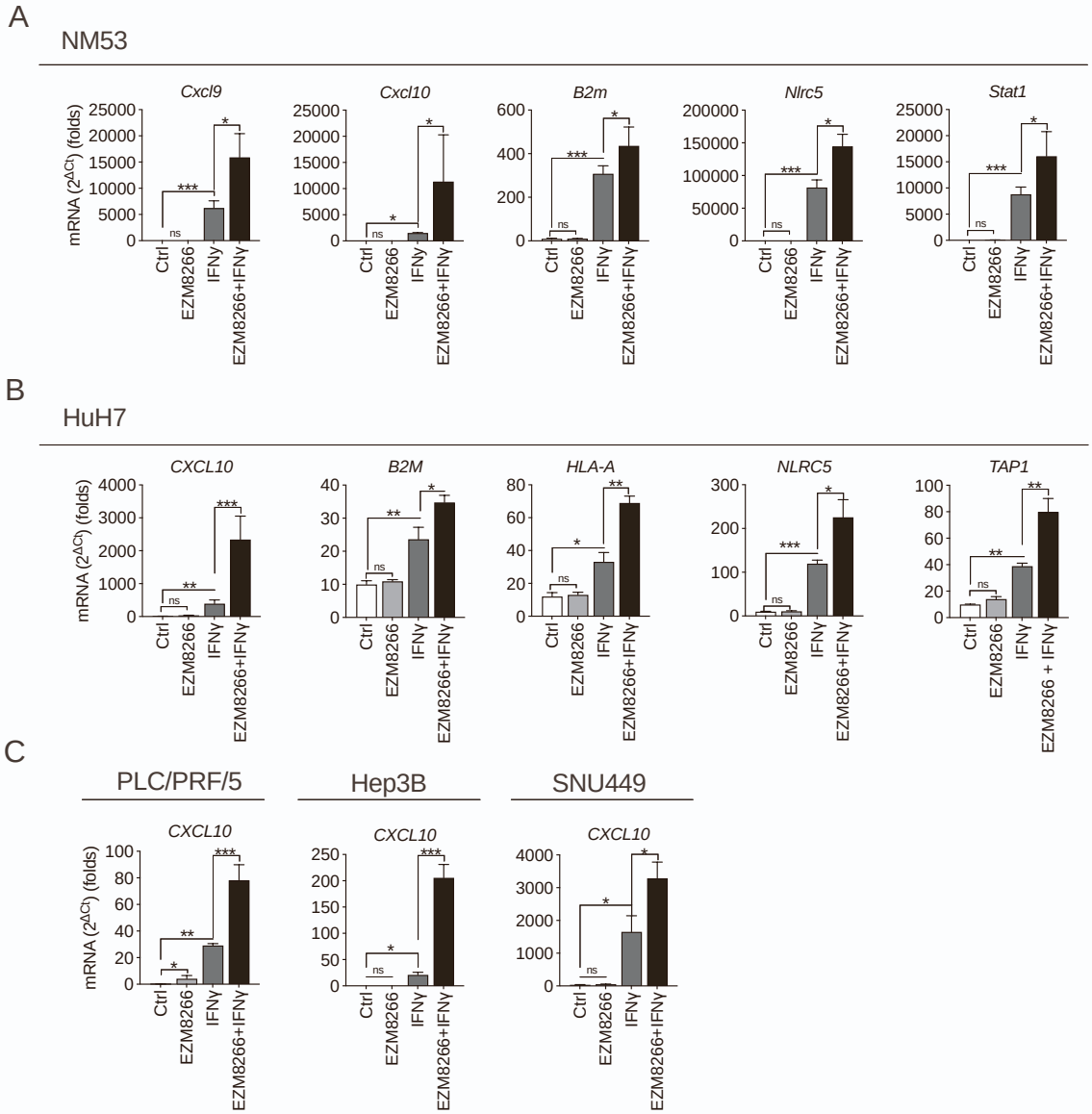

Figure S3. ***G9a inhibition with EZM8266 enhances the immunogenicity of HCC cells. NM53.*** (A) and HuH7 (B) cells were pretreated for 48 h with EZM8266 (5 mM) and then with INFg (75 U/mL) for another 24 h as indicated (n=3). (C) *CXCL10* mRNA expression levels of human HCC cell lines PLC/PRF/5, Hep3B and SNU449 cells treated with EZM8266 (5 mM) for 24 h, followed by 24 h of IFNγ stimulation (75 U/mL) as indicated (n=3). The expression of the indicated genes was analyzed by qPCR. Related to Figure 4. Data are represented as mean +/- SEM. * *p<0.05*, ** *p<0.01*, *** *p<0.001*, **** *p<0.0001*. All the replicates represent biological replicates.

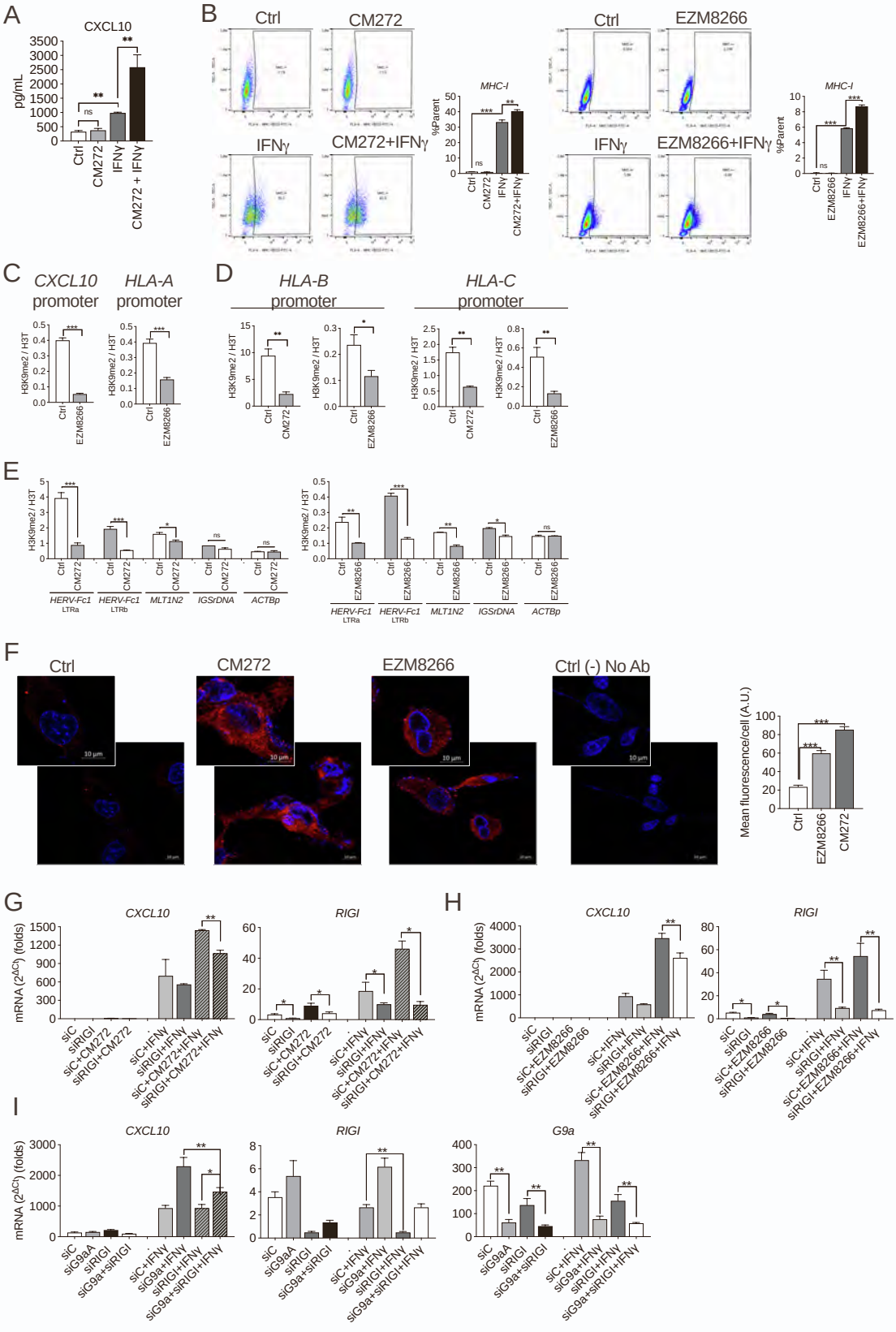

Figure S4. ***G9a inhibition potentiates the immunogenic effects of INFg in HCC cells.*** Effect of CM272 on INFg-triggered CXCL10 production in murine NM53 HCC cells. Cells were treated with CM272 for 48 h or with CM272 for 24 h and then with INFg (75 U/mL) for another 24 h, or with INFg alone for 24 h. CXCL10 protein levels were measured by ELISA in cells' conditioned media (n=3). (B) Effect of G9a inhibition with CM272 or EZM8266 on the expression of MHC class I complex protein (MHC-I) on the surface of NM53 cells. Cells were treated with INFg and CM272 or EZM8266 as indicated in panel A, and MHC-I levels were determined by FACS analysis (n=3). (C) ChIP analyses of H3K9me2 levels in the proximal promoter regions of CXCL10 and HLA-A genes in HuH7 cells treated with EZM8266 (5 mM, 48 h) (n=3). (D) ChIP analyses of H3K9me2 levels in the proximal promoter regions of HLA-B and HLA-C genes in HuH7 cells treated with CM272 (400 nM) or EZM8266 (5 mM, 48 h) (n=3). (E) Quantification of H3K9me2, H3K4me3, and H3K27ac levels by ChIP-qPCR at LTR regions of HERV-Fc1 (Fc1 LTRa and b) and MLT1N2. The intergenic spacer region of the 35S ribosomal DNA genes (IGS rDNA) and the promoter region of b-actin (ACTBp) were used as controls (n=3). (F) Immunofluorescence analyses of dsRNA in HuH7 HCC cells treated with CM272 (24 h) or EZM8266 for (48 h). Righ panel shows a control without primary antibody (n=3). (G) qPCR analysis of CXCL10 and RIGI in HuH7 cells transfected with RIGI-specific siRNAs for 24 h, treated with CM272 (400 nM) for 24 h and stimulated with or without IFNg for other 24 h more. (H) qPCR analysis of CXCL10 and RIGI in HuH7 cells transfected with RIGI-specific siRNAs for 24 h, treated with EZM8266 (5 mM) for 24 h and stimulated with or without IFNg for other 24 h more (n=3). (I) qPCR analysis of CXCL10, RIGI and G9a expression in HuH7 cells transfected with G9a, RIGI, or specific siRNAs combinations (siG9a + siRIGI) and control siRNAs (siC) for 24 h and stimulated with or without IFNg for other 24 h more (n=3). Related to Figure 5. Data are represented as mean +/- SEM. * *p<0.05*, ** *p<0.01*, *** *p<0.001*. All the replicates represent biological replicates.

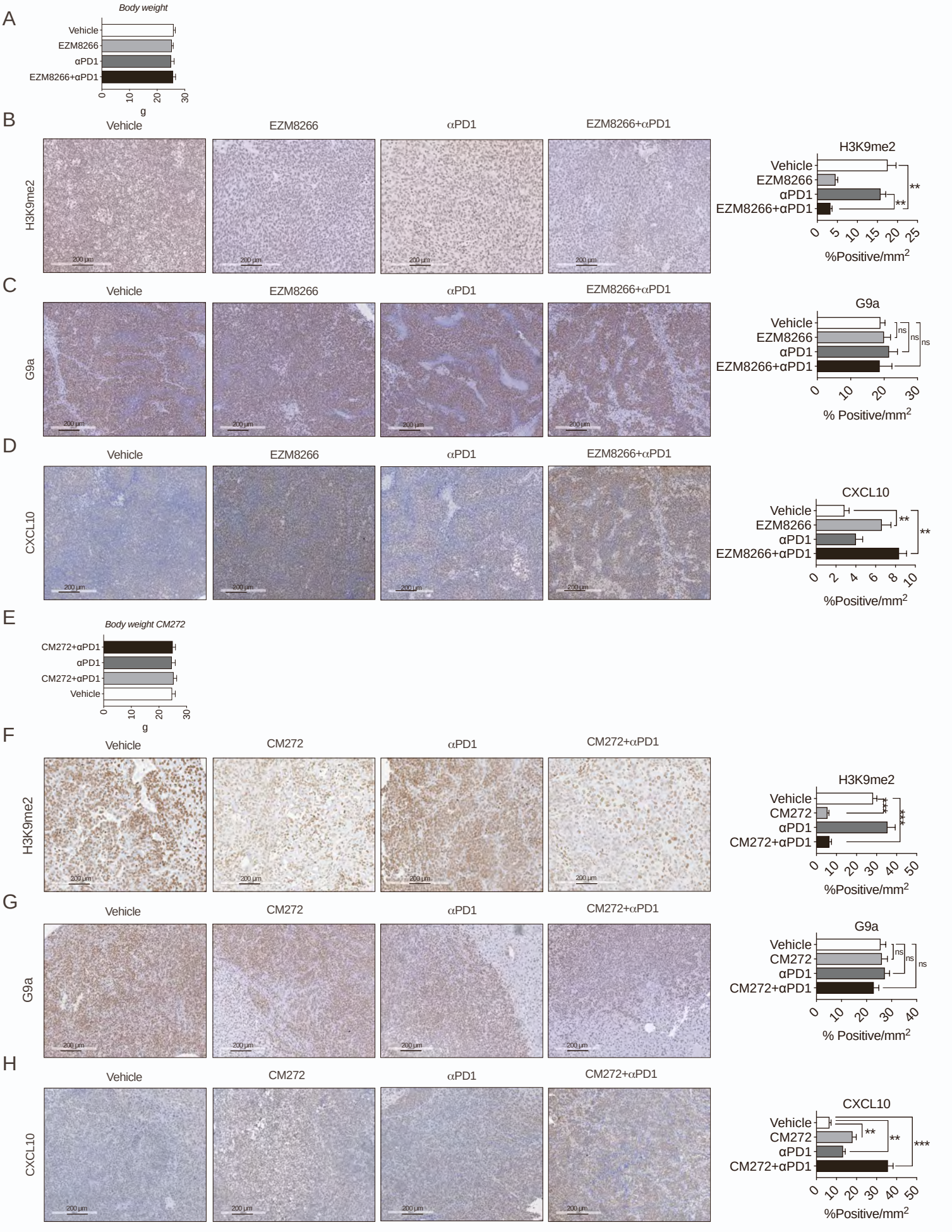

Figure S5. ***In vivo G9a inhibition effects with EZM8266 and CM272 alone or in combination with ICI.*** (A, E) Body weight of animals in different experimental groups (n=10/group) (B, F). Representative images showing the immunohistochemical detection of H3K9me2 and quantification in the different groups of mice at the end of treatments. (C, G) Representative images showing the immunohistochemical detection of G9a and quantification in the different groups of mice at the end of treatments. (D, H) Representative images showing the immunohistochemical detection of CXCL10 and quantification in the different groups of mice at the end of treatments. Scale bars, 200 µm. Related to Figures 6 and 7. Data are represented as mean +/- SEM. * *p<0.05*, ** *p<0.01*, *** *p<0.001*, *ns, non significant*.

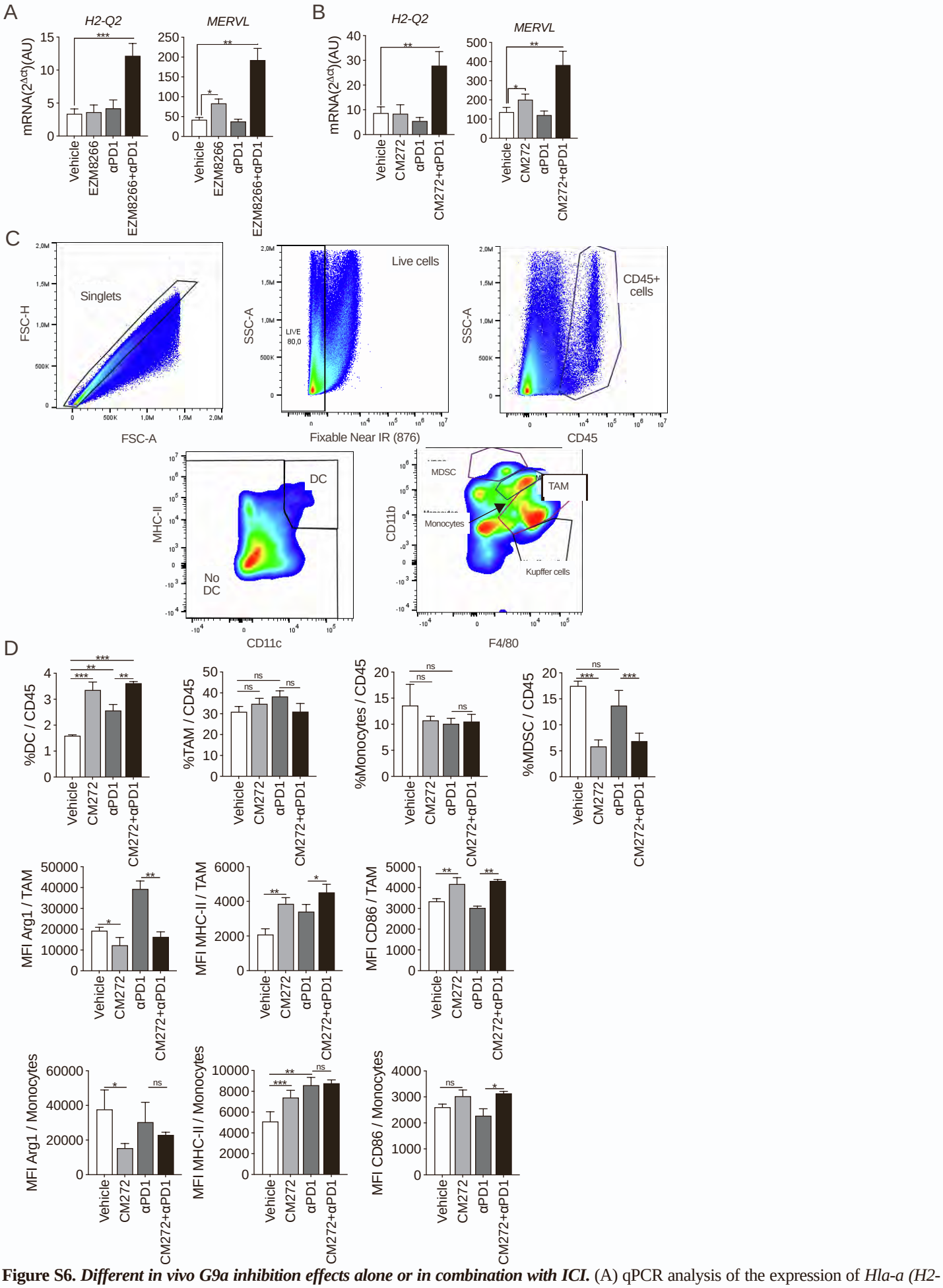

Figure S6. ***Different in vivo G9a inhibition effects alone or in combination with ICI.*** (A) qPCR analysis of the expression of *Hla-a (H2-Q2)* and *MERVL* in tumor tissues from mice treated with Vehicle, EZM8266, α-PD1 and the combination of EZM8266 and α-PD1. (n=10/group) (B) qPCR analysis of the expression of *Hla-a (H2-Q2)* and *MERVL* in tumor tissues from mice treated with Vehicle, CM272, α-PD1 and the combination of CM272 and α-PD1. (n=10/group) (C) Gating strategy for the identification and study of myeloid cells in PM299L orthotopic tumors. Orthotopic HCC PM299L tumors were obtained from mice at after different treatments. After digestion and homogenization, cells were stained with antibodies to identify myeloid cells, and different myeloid subsets were defined according to the gating strategy shown. (D) Flow cytometry analyses of tumor infiltrating cells obtained from mice treated with Vehicle, CM272, aPD1 and CM272 + aPD1 combinations. Percentage of DC, TAM, Monocytes and MDSCs cells. Expression levels (MFI) of Arg1, MHC II and CD86 in each TAM and Monocytes subsets (n=5). Related to Figure 7. Data are represented as mean +/- SEM.* *p<0.05*, ** *p<0.01*, *** *p<0.001*, *ns, non significant.*

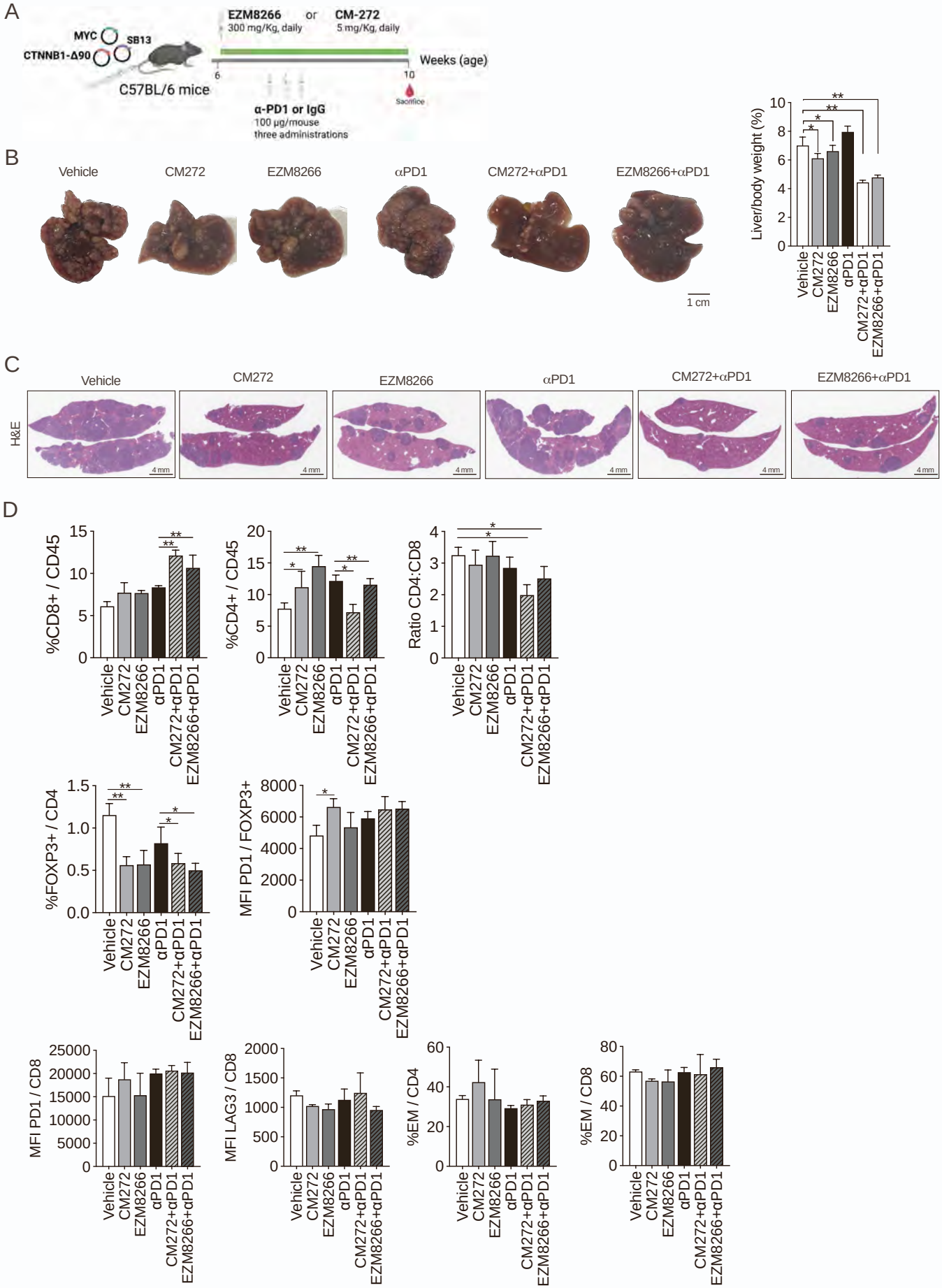

Figure S7. ***G9a targeting with different tool compounds increases the efficacy of ICI in a genetic HCC model.*** (A) Experimental protocol for the study of the antitumoral effects of CM272 and EZM8266 in combination with ICI in a HCC model developed by hydrodynamic tail vein injection of pT3-EF1a-MYC (MYC), the CMV-SB13 (SB13) vector and a transposon vector expressing activated b-catenin (CTNNB1-Δ90) in immunocompetent mice (n=10/group) (B) Representative images of tumors in the different groups of mice at the end of treatments. Scale barrs, 1 cm. Quantitation of liver index in each experimental group are indicated. (C) Histological evaluation of tumor growth (tumor area) in the different treatment groups. Representative images of H&E-stained liver and tumor tissues are shown. Scale barrs, 4 mm. (D) Flow cytometry analyses of tumor infiltrating cells obtained from the different experimental groups (n=5). Related to Figure 7. Data are represented as mean +/- SEM. * *p<0.05*, ** *p<0.01*, *** *p<0.001*, *ns, non significant.* All the replicates represent biological replicates.

Table S1. Publicly available gene signatures and gene sets used in the study.

Name	Study	Reference
Wnt-βcatenin Activation signature	Lachenmayer A, et al. Clin Cancer Res 2012;18:4997-5007	32
Immune enrichment score	Yoshihara K, et al. Nat Commun 2013;4:2612	68
Activated CD8 T cells	Charoentong P, et al. Cell Rep 2017;18:248–262	29
Activated CD4 T cells	Charoentong P, et al. Cell Rep 2017;18:248–262	29
M1 macrophages	Davoli T, et al. Science 2017;355:eaaf8399	30
Tertiary lymphoid structure (TLS)	Cabrita R, et al. Nature 2020;577:561–565	31
Cytolytic activity	Rooney MS, et al. Cell 2015;160:48–61	67
IFN signature (18-gene)	Ayers M, et al. J Clin Invest 2017;127:2930–2940	24
Inflammatory signature	Sangro B, et al. J Hepatol 2020;73:1460–1469	28
IFNAP signature	Haber PK, et al. Gastro 2023	23